Sensorless vector control of PMSG for wind turbine applications

MASTER THESIS
PED4-1038B

INSTITUTE OF ENERGY TECHNOLOGY
AALBORG UNIVERSITY

03rd JUNE 2009

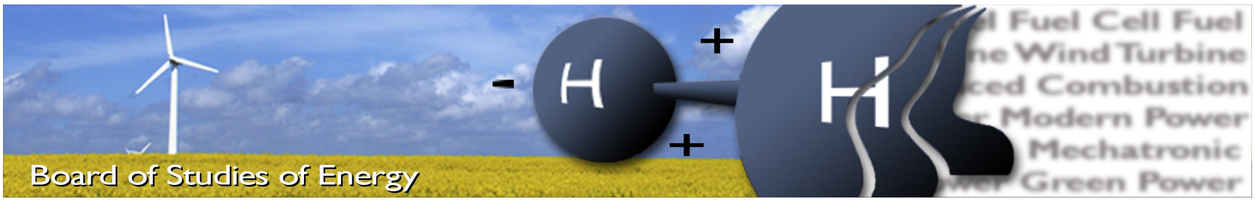

Title:	Sensorless vector control of PMSG for wind turbine applications
Semester:	4^{th}
Semester theme:	Master Thesis
Project period:	01.02.09 to 03.06.09
ECTS:	30
Supervisors:	Florin Iov
	Uffe Jakobsen
Project group:	PED4-1038B

SYNOPSIS:

This project deals with the design of a sensorless Field Oriented Control (FOC) on a surface mounted permanent magnet synchronous generator (PMSG) for wind turbine applications. In order to be able to implement the control in laboratory, a 2.2[kW] machine is used. The FOC is first simulated in Matlab/Simulink, using the measured speed and position. A method for estimating the rotor position is investigated and also tested in simulation. The simulation results show good performance for both sensored and sensorless FOC. The sensored FOC is tested in dSpace and the results prove that the control is working. The position estimation method could not be implemented in laboratory. The main conclusions are taken in the final chapter.

Maria Oana Mora

Copies:	- 3
Pages, total:	- 64
Appendix:	- 4
Supplements:	- 3 CDs

By signing this document, each member of the group confirms that all participated in the project work and thereby all members are collectively liable for the content of the report.

Preface

The present report is prepared by Maria Oana Mora, student in the 4^{th} Semester, at Power Electronics and Drives. The project, with the title *Sensorless vector control of PMSG for wind turbine applications* was a proposal from Siemens Wind Power. The main idea of the project is to control a permanent magnet synchronous machine without using a sensor.
The project is documented in a main report and appendixes. The main report can be read as a self-contained work, while the appendixes contain details about measurements or other data. In this project the chapters are consecutive numbered whereas the appendixes are labeled with letters.

Figures, equations and tables are numbered in succession within the chapters. For example, Fig. 3.2 is the second figure in chapter 3.

The references are written with the Harvard method with [Author,Year]. More detailed information about the sources is given at the end of the main report in Bibliography.

Matlab/Simulink is used for all the simulations. For implementation in the real time system a dSpace setup is used. The software used as an interface between the user and dSpace is Control Desk.

A CD-ROM containing the main report and appendixes is attached to the project.

I would like to thank my supervisors, Florin Iov and Uffe Iakobsen, for all their support in helping me with the problems that I confronted.

The author

Contents

List of Figures

Nomenclature

B	- Viscous friction
D_a, D_b, D_c	- Duty cycles
e	- Back-emf voltage
f	- Nominal frequency of the machine
f_s	- Sampling frequency
K_e	- Voltage constant
k_a	- Antiwindup gain
$k_{pi_{q,d}}, T_{i_{q,d}}$	- Proportional and intergral gain of q,d axis current controller
k_{p_ω}, T_ω	- Proportional and intergral gain of the speed controller
L_d, L_q	- d,q axis stator inductances
${L^s}_s$	- Stator inductance in the stationary reference frame
$i_a, i_b, i_c,$	- Line currents
i_α, i_β	- Stator currents in α, β stationary reference frame
$\hat{i}_\alpha, \hat{i}_\beta$	- Estimated stator currents in α, β stationary reference frame
$\Delta i_\alpha, \Delta i_\beta$	- Current errors in α, β stationary reference frame
i_{sd}, i_{sq}	- Stator currents in d,q rotor reference frame
J	- Moment of inertia
M_p	- Overshoot
n	- Rated speed of the motor in [rpm]
ω_e	- Electrical speed in [rad/sec]
ω_r, ω_r^*	- Electrical and reference speed in [rot/min]
ω_m	- Mechanical speed
p	- Number of poles
p_b	- Number of pair poles
P, Q	- Active, reactive power
Ψ_α, Ψ_β	- Flux linkages in α, β stationary reference frame
$\hat{\Psi}_\alpha, \hat{\Psi}_\beta$	- Estimated flux linkages in α, β stationary reference frame
Ψ_d, Ψ_q	- Flux linkages in d,q rotor reference frame
Ψ_m	- Permanent magnet flux
R_s, L_s	- Stator resistance, stator inductance
S_a, S_b, S_c	- Switching status for each leg of the converter
T_e	- Electromagnetic torque
T_d	- Dry friction torque
T_L	- Load torque
τ_q, τ_d	- q,d electrical time constant
t_0, t_7	- Application time of zero vectors
$t_1 - t_6$	- Application time of active vectors
θ_r	- Load angle
$\hat{\theta}_r$	- Estimated rotor position
$\hat{\theta}_{rp}$	- Predicted rotor position
$\Delta\theta_\alpha, \Delta\theta_\beta$	- Position errors in α, β stationary reference frame
T_{PWM}	- Switching frequency

t_s	- Settling time
T_s	- Sampling time
T_{si}	- Equivalent time constant
$T_{\omega c}$	- Time constant of the speed filter
$u_{a0}, u_{b0}, u_{c0},$	- Phase voltages
u_α, u_β	- Stator voltages in α, β stationary reference frame
U_{DC}, I_{DC}	- DC link voltage, current
$\bar{U^*}$	- Reference voltage space vector
u_{sd}, u_{sq}	- Stator voltages in d,q rotor reference frame
$\vec{u_s}, \vec{i_s}, \vec{\Psi_s}$	- Space vectors of the stator voltage, current and flux linkage

ABREVIATIONS

AC	Alternative Current
DC	Direct Current
DFIG	Doubly Fed Induction Generator
DSP	Digital Signal Processor
FOC	Field Oriented Control
IPMSG	Interiour Permanent Magnet Synchronous Generator
MRAS	Model Reference Adaptive Observer
OM	Optimal Modulus
OSM	Optimum Symmetric Method
PI	Proportional Integral
PM	Permanent Magnet
PMSG	Permanent Magnet Synchronous Generator
PMSM	Permanent Magnet Synchronous Machine
PWM	Pulse Width Modulation
RTI	Real Time Interface
SPMSM	Sourface Mounted Permanent Magnet Synchronous Machine
SVM	Space Vector Modulation
VSC	Voltage Source Converter

1
Introduction

The purpose of this chapter is to present an introduction to the proposed project. The chapter begins with an introduction to the subject. The problem formulation and the objective are presented next. The report structure is described at the end.

1.1 Background of Wind Power Systems

In recent years there has been an increasing awareness about the climate change (global warming) and the harmful effects that the emissions of carbon have. This created a higher demand for clean and sustainable energy sources like: wind, sea, sun, biomass etc. The wind energy has experienced the biggest growth in the past 10 years. [Patel,2006] This is because wind energy is a pollution-free resource, has an inexhaustible potential and also because of its increasingly competitive cost. According to World Wind Energy Association the total installed capacity of wind energy increased, from 1997 to 2007, with 86.374 MW , as shown in Fig.1.1.

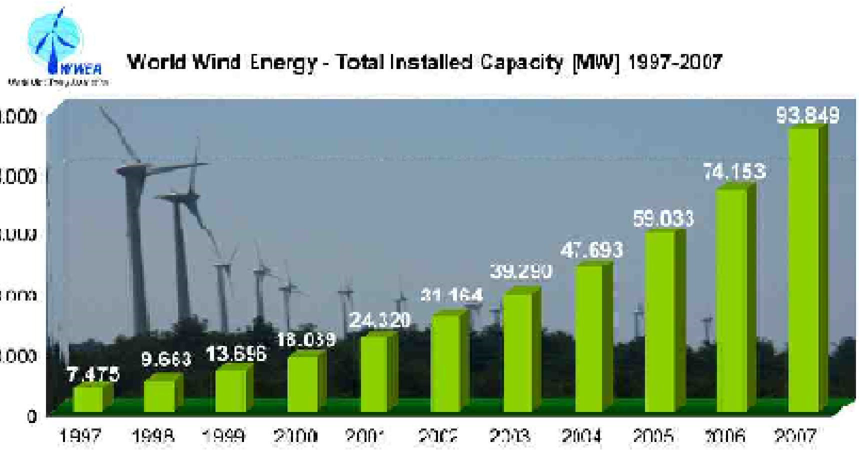

Figure 1.1: *The total wind energy installed capacity - courtesy of World Wind Energy Association*

The size of the wind turbine installations has also grown from 300 KW in the early 1990, up to 5 MW capacity range in our days.

The main drawback of the wind is that it is irregular in occurrence. The problem becomes how to maximize the energy capture from the wind.

In terms of generators for wind power-application, there are two main classes considering the speed: constant and variable speed. The constant speed wind turbines and induction generators were often used, in the early stages of wind power development. Some of the disadvantages of the fixed speed generators is the low efficiency, poor power quality, high mechanical stress but also that by having a fixed speed operation the maximum coefficient of performance is obtained only at a particular wind speed.[Yin,2007]

In the past years because of the development of power electronics and their falling costs, the variable speed operation became the most attractive option. By running the wind turbine generator in variable speed, variable frequency mode, the maximum power can be extracted, at low and medium wind speeds. The theory and field experience indicate that the variable-speed operation yields 3-4% more energy, per year, than with the fixed-speed operation.[Patel,2006] In Fig.1.2 the operating points for a variable speed wind generator with power limited by a constant speed and by a converter, are presented.

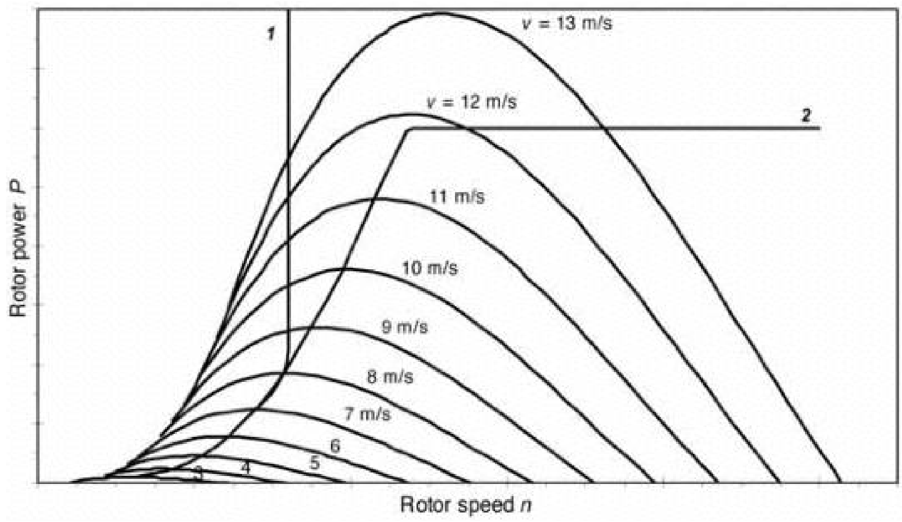

Figure 1.2: *Operating points for a variable speed wind generator with power limited by 1-Constant speed or 2-Converter [Quaschning,2006]*

As shown in the figure, at high wind speeds it is necessary to limit the power.

1.2 Problem formulation

The most widely used variable-speed wind turbine topology, in present, is the doubly fed induction generator (DFIG) wind turbine, equipped with a partial-scale power converter. However, the topology with PM synchronous generator and full-scale converter has also an increasing market share today. Compared with the induction generator, the permanent magnet synchronous generator is more efficient, smaller in size and easier to control. [Senjyu,2007] The efficiency of the PMSG wind turbine, was assessed to be higher than other variable speed wind turbine concepts. Meanwhile, PMSG presents also some disadvantages like high costs for the permanent magnets and a fixed excitation, which cannot be changed according to the operational point.[Li,2008] The PMSG can be operated in variable speed, so that the maximum power can be extracted. Traditionally, wind turbine generators are operating best at high speeds and require step-up gearboxes. A multipole direct driven PM generator, connected to the grid through a full scale converter, can be operated at low speeds, so that the gearbox can be omitted. Direct driven applications are increasingly applied due to the fact that a direct driven generator has reduced overall size, lower installation and maintenance cost, a flexible control method and quick response to wind fluctuation and load variation. [Fatu,2008] The full scale converter consists of a back-to-back voltage source converter(VSC) - a generator side converter and the grid side converter, connected through a DC link. The capacitor decoupling, offers the possibility of separate control for each converter. The grid side converter controls the power flow in order to keep the DC-link voltage constant, while the generator side converter controls the torque and the speed. Also having this configuration the PMSG is more isolated from the grid, which makes possible to control the fault currents in the PMSG, that arise form external faults in the grid. [Fatu,2008] In Fig.1.3, a general presentation of a direct driven PMSG with full scale converter is presented. Being

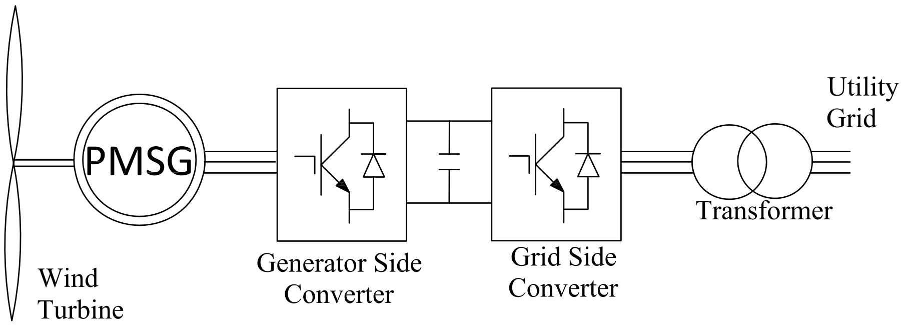

Figure 1.3: *Wind Energy Conversion System*

an increasing utilized topology, accurate modeling and control of this wind turbine concept has a very big importance. One of the necessary requirements in controlling the PMSG is to identify the rotor position and speed. They can be determined either by using speed or shaft position sensors, or they can be estimated. Using a sensor implies several drawbacks like the drive cost, reliability, which makes the sensorless control an attractive option. The problem formulation becomes:

Without using a sensor can an accurate control be implemented on a surface mounted PMSG for wind turbine applications?

1.3 Objective

The objective of this project is to implement a sensorless control structure for the generator side voltage source converter. For verification, a sensored control is also implemented. In order to have a laboratory implementation, the control is applied on a 2.2[KW] generator. The control is simulated in Matlab/Simulink and afterwards is tested in laboratory.

The main goals of the project are summarized below:

- design a sensored control structure for a surface mounted PMSG;

- investigate methods used for the sensorless control;
- choose a method and investigate its performances on a 2.2[KW] generator in Matlab/Simulink;
- laboratory implementation of the sensored control in dSpace;
- laboratory implementation of the sensorless control in dSpace;
- if the sensorless method shows satisfactory results, implementation of the sensorless control on a 2-3[MW] generator.

1.4 Project limitation

Due to the time limitation and the complexity of the considered system, some limitations are considered in the development of this project:

- The wind model, wind turbine model and the drive train model are not considered;
- The grid side converter control is not implemented, the focus is only on the generator side converter control;
- The sensorless control is not investigated at low speeds (below 500[rpm]).

1.5 Report structure

The present report consists of 6 chapters. In the first chapter a presentation of the report is made. At the beginning an introduction to the subject is presented. The problem formulation, the objective and the project limitations are also presented. The purpose of the second chapter is to describe the system and its components. The converter, the control strategy for the converter and the machine are shortly described. The control strategy, Field Oriented Control (FOC), is presented in Chapter 3. Here the controllers design and the control performances are shown. Chapter 4 starts with a presentation of methods for position and speed estimation. One method is chosen to be simulated and the results are presented. In Chapter 5, the laboratory work is presented and the results are shown and discussed. The conclusions are taken in Chapter 6.

2

System Description

This chapter begins with a general presentation of the system. Next the system components are shortly described. First, the converter and the Space Vector Modulation (SVM) strategy for determining the duty cycles, are introduced. A short description of the permanent magnet synchronous machine is presented in the next section. In order to be able to test the control in laboratory, the simulation is made on a 2.2KW PMSM. At the end of the chapter, the simulation results are presented.

2.1 General presentation

The general presentation of the actual system is presented in Fig.2.1

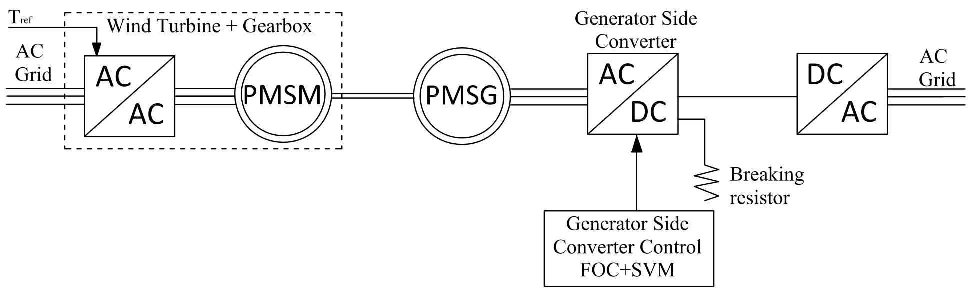

Figure 2.1: *Overall system presentation*

As it can be seen in Fig.2.1, the wind turbine and the gear box are replaced by a permanent magnet synchronous machine (PMSM) which is torque controlled. The generator side converter is controlled using Space Vector Modulation strategy.

In the followings the converter, the SVM strategy and the PMSG are presented.

2.2 Converter

The equivalent circuit of a voltage source converter is presented in Fig.2.2. As it can be seen in the figure, a three phase converter has 6 semiconductors (IGBTs) displayed in three legs: a,b and c. The 6 semiconductors are considered as ideal switches. Only one switch on the same leg can be conducting at the same time.

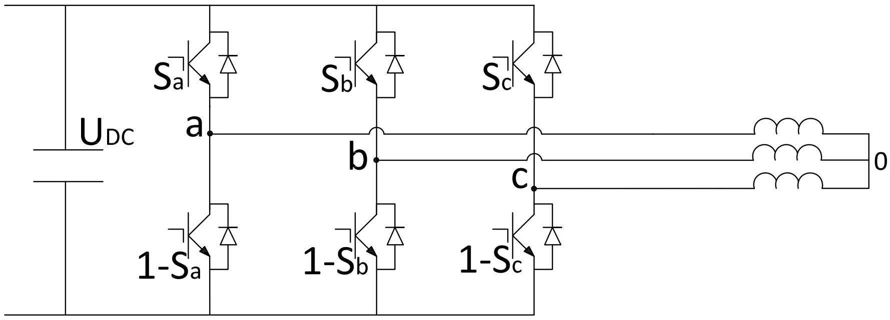

Figure 2.2: *VSC with ideal switches*

In the figure, S_a, S_b, S_c are variables which represent the switching status for each leg. S can only have two values: 1 for the conduction state and 0 for the block state. The desired output voltages are obtained by programming the duty cycles of the 6 IGBTs. In Eq.2.1, the phase voltages are calculated using the DC voltage and the duty cycles D_a, D_b, D_c.

$$\begin{aligned} u_{a0} &= \frac{U_{DC}}{3}(2D_a - D_b - D_c) \\ u_{b0} &= \frac{U_{DC}}{3}(-D_a + 2D_b - D_c) \\ u_{c0} &= \frac{U_{DC}}{3}(-D_a - D_b + 2D_c) \end{aligned} \tag{2.1}$$

where,

u_{a0}, u_{b0}, u_{c0} - phase voltages;

U_{DC} - DC voltage.

The DC link current can be expressed as:

$$i_{DC} = \begin{bmatrix} D_a & D_b & D_c \end{bmatrix} \cdot \begin{bmatrix} i_a \\ i_b \\ i_c \end{bmatrix}$$

where,

i_a, i_b, i_c - line currents.

2.3 Space Vector Modulation (SVM)

The strategy used for determining the duty cycles is SVM. The space vector strategy, which is based on space vector representation of the converter AC side voltage, has become very popular because of its simplicity.[Kazmierkowski,2002]. This technique provides an accurate control of voltage amplitude and frequency, and is suitable for variable torque loads and for large power drives. Also in the SVM there are no separate modulators for each phase as in carrier-based PWM.

Based on the switches status, there are only 8 possible different output voltage status: 6 of them are active and produce non-zero output voltage and the other two produce zero voltage output. Each voltage output status may correspond to a space vector. SVM uses the stationary α, β reference frame. The reference voltage space vector $\bar{U^*}$ is defined as follows:

$$\bar{U^*} = u_\alpha + ju_\beta = \frac{2}{3}(u_{aref} + e^{j\frac{2\pi}{3}}u_{bref} + e^{-j\frac{2\pi}{3}}u_{cref}) \tag{2.2}$$

where $u_{aref}, u_{bref}, u_{cref}$ are the reference phase voltages.

The active vectors divide the plane in six sectors, where the reference vector $\bar{U^*}$ is obtained by switching on (for the proper time) two adiacent vectors. In Fig.2.3 the reference vector is located in sector 1, which means that is defined by the state voltages $\bar{U}_1$ and $\bar{U}_2$. $\bar{U}_1$ is the state voltage produced by the state [1 0 0], which means that the upper switch of the first leg, and the lower switches of the second and third legs of the VSC, are conducting. In the figure, T_{PWM} is the switching frequency and α is the phase angle of $\bar{U^*}$.

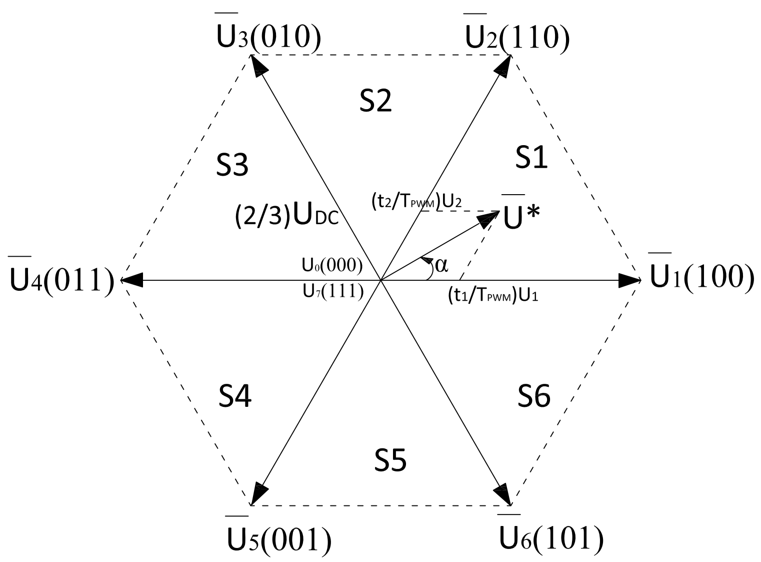

Figure 2.3: *Space vector representation of 3 phase converter*

The maximum length of the $\bar{U^*}$, for each α angle is $\bar{U^*}_{max} = U_{DC}/\sqrt{3}$.[Kazmierkowski,2002]

In Fig.2.4, the switching states occur as: [0 0 0], [1 0 0], [1 1 0], [1 1 1] to reduce the number of switching commutations. In SVM the zero states are simmetrical[Kazmierkowski,2002]:

$$t_7 = t_0 = \frac{T_{PWM} - t_1 - t_2}{2} \tag{2.3}$$

where, $t_0, t_1, ..., t_7$ are the time durations of the applied vectors.

$\bar{U^*}$ in sector 1 can be calculated as in Eq.2.4.

$$\bar{U^*} = \bar{U}(100)\frac{t_1}{T_{PWM}} + \bar{U}(110)\frac{t_2}{T_{PWM}} \tag{2.4}$$

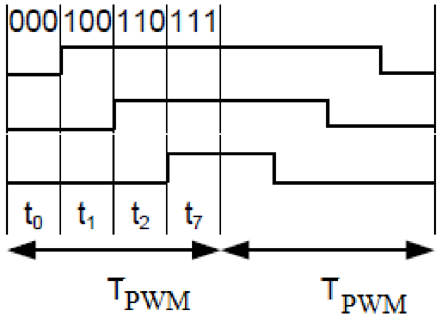

Figure 2.4: *State sequence*

where,

$$\bar{U}(100) = \frac{2}{3}U_{DC} \tag{2.5}$$

$$\bar{U}(110) = \frac{2}{3}U_{DC}(\frac{1}{2} + j\frac{\sqrt{3}}{2}) \tag{2.6}$$

From Eq.2.4, considering $\bar{U^*} = U^*(cos\alpha + jsin\alpha)$, and splitting into real and imaginary parts, the time durations t_1 and t_2 can be calculated as [Kazmierkowski,2002]:

$$t_1 = \sqrt{3}\frac{U^*}{U_{DC}}T_{PWM}sin(\frac{\pi}{3} - \alpha) \tag{2.7}$$

$$t_2 = \sqrt{3}\frac{U^*}{U_{DC}}T_{PWM}sin\alpha \tag{2.8}$$

Having t_1 and t_2 calculated, the residual sampling time is reserved for zero vectors U_0 and U_7. The condition is that $t_1 + t_2 \leq T_{PWM}$. The duty cycles, for sector 1 can be calculated like in the followings:

$$D_a = \frac{t_1 + t_2 + t_0/2}{T_{PWM}} \tag{2.9}$$

$$D_b = \frac{t_2 + t_0/2}{T_{PWM}} \tag{2.10}$$

$$D_c = \frac{t_0/2}{T_{PWM}} \tag{2.11}$$

The expressions for the other sectors can be calculated in the same way. Having the duty cycles the switching signals, for the converter IGBTs, are obtained from the PWM generator.

The duty cycles, from the simulation, for the desired output voltage (285[V] phase voltage) are shown in Fig.2.5.

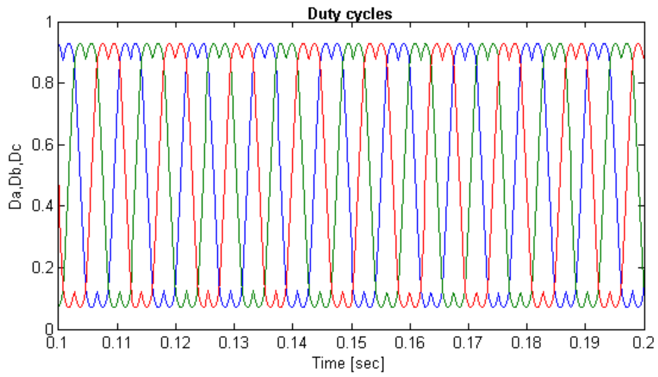

Figure 2.5: *Duty cycles*

2.4 Permanent Magnet Synchronous Generator(PMSG)

The PMSG is a regular Synchronous Machine, where the DC excitation circuit is replaced by permanent magnets, by this eliminating the brushes. Without the brushes and the slip rings, and because of the permanent magnets, the PMSG has a smaller physical size, a low moment of inertia which means a higher reliability and power density per volume ratio. Also by having permanent magnets in the rotor circuit, the electrical losses in the rotor are eliminated. Due to the mentioned advantages, the PMSG are becoming an interesting solution for wind turbine applications.

However, the disadvantages of the permanent magnet excitation are high costs for permanent magnet materials and a fixed excitation, which cannot be changed according to the operational point.

The PMSG can be classified according to the rotor configuration:

- *Interior magnet type (IPMSG)* For this configuration, the magnets are buried inside the rotor. The interior magnet PMSG usually presents magnetic saliency. The d-axis inductance is smaller than the q-axis inductance ($L_d < L_q$), because the effective airgap of the d-axis is bigger than the q-axis airgap. This results in a component of reluctance torque in addition to the torque produced by the magnet. Because of this, the rotor position is much easier to detect.

- *Surface mounted magnet type (SPMSG)* The SPMSG has the magnets mounted on the surface of the rotor. As the permeability of the permanent magnets is approximately equal to 1, permanent magnets act like air in magnetic circuits. This means that the air gap is very large and constant. The d- and q-axis inductances are nearly identical and the saliency ratio ($\xi = Lq/Ld$) is 1. Therefore no reluctance torque occurs.

One advantage of the SPMSG is that the sourface mounted magnets lead to a very simple rotor design with a low weight.[Grauers,1996]

In this project the control is implemented on a surface mounted, 2.2 KW, PMSG. The parameters of the machine are presented in Table2.1

Parameter	Symbol	Value	Unit
Nb. of poles	P	6	-
Frequency	f	87.5	[Hz]
Stator resistance	R_s	1.906	[Ω]
d-axis stator inductance	L_d	30.31	[mH]
q-axis stator inductance	L_q	38.36	[mH]
Voltage constant	K_e	495,3	-
Moment of inertia	J	0.002	$[kg \cdot m^2]$
Viscous friction	B	0.0028	

Table 2.1: *PMSM parameters*

The electrical parameters presented in Table 2.1 were read from the machine plate. The mechanical parameters, moment of inertia, J, and viscous friction, B, were measured. The measurements are described in Appendix A.

2.4.1 Mathematical model

In order to be able to test the implemented control, the PMSG is simulated in Matlab/Simulink. For the machine simulation, a mathematical model is developed. The model is extracted from [Vas,1998] and is presented in the followings. The model is derived from the space vector form of the stator voltage equation, Eq.2.12:

$$\vec{u_s} = R_s\vec{i_s} + \frac{d}{dt}\vec{\Psi_s} \tag{2.12}$$

where,

R_s - stator resistance;

$\vec{u_s}$ and $\vec{i_s}$ - space vectors of the stator voltages and currents;

$\vec{\Psi_s}$ - space vector of the flux linkage.

In order to be able to simulate the PMSG in Matlab/Simulink the dq model is needed. By transforming from a,b,c system into d,q system, the expression of electrical equations are

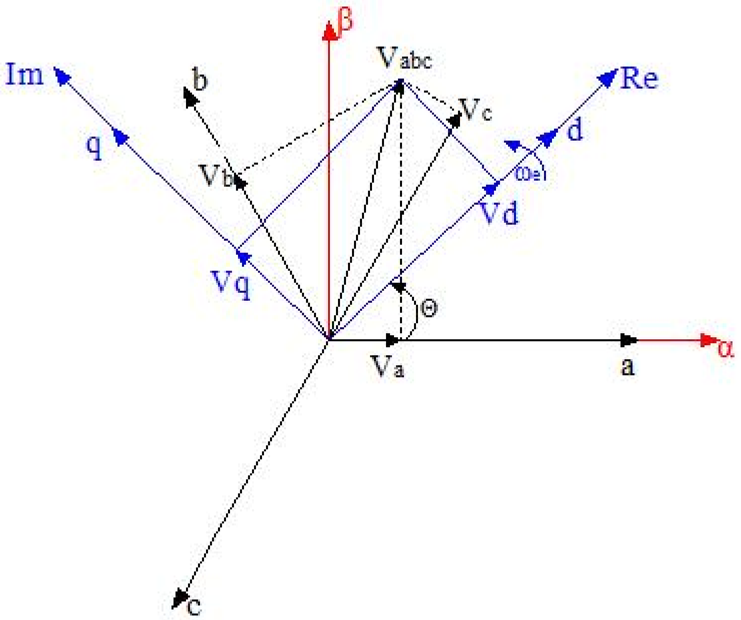

Figure 2.6: *Reference frames in a 3 phase circuit*

greatly simplified and also the time and position dependencies are being removed. The abc to dq transformation is shown in Fig. 2.6.

Voltage equations in d,q system:

$$u_{sd} = R_s i_{sd} + \frac{d\Psi_d}{dt} - \omega_e \Psi_q \tag{2.13}$$

$$u_{sq} = R_s i_{sq} + \frac{d\Psi_q}{dt} + \omega_e \Psi_d \tag{2.14}$$

where,

u_{sd}, u_{sq} - d,q axis stator voltages;

i_{sd}, i_{sq} - d,q axis stator currents;

R_s - stator resistance;

Ψ_d, Ψ_q - d,q axis stator flux linkages;

ω_e - electrical speed in rad/sec.

Flux equations in d,q system

The d,q fluxes equations are presented in Eq.2.15 and Eq.2.16.

$$\Psi_d = L_d i_{sd} + \Psi_m \tag{2.15}$$

$$\Psi_q = L_q i_{sq} \tag{2.16}$$

where,

L_d, L_q - d,q axis inductances;

Ψ_m - permanent magnet flux linkage.

Torque equation
The electromagnetic torque can be derived from the expression of electromagnetic power which is:

$$P_{em} = \omega_m T_e = \frac{3}{2}\omega_e(\Psi_d i_{sq} - \Psi_q i_{sd}) \tag{2.17}$$

ω_m is the mechanical speed of the rotor. The relation between the electrical and mechanical speed is:

$$\omega_e = \frac{p}{2}\omega_m \tag{2.18}$$

where, p - number of poles

This means that the expression for the electromagnetic torque, in d,q coordinate system, is as shown below:

$$T_e = \frac{3}{2}\frac{p}{2}(\Psi_d i_{sq} - \Psi_q i_{sd})\text{[AC Machines,2008]} \tag{2.19}$$

By replacing the flux expressions, from equations 2.15 and 2.16, into the torque equation, the following equation is obtained:

$$T_e = \frac{3}{2}\frac{p}{2}(\Psi_m i_{sq} + (L_d - L_q) i_{sd} i_{sq})\text{[AC Machines,2008]} \tag{2.20}$$

The first term is the interaction torque between the magnetic field and the i_{sq} current and the second term is the 'reluctance torque'. As previously said the d,q inductances for the surface mounted PMSM are equal, so **the torque relation for this kind of machine is:**

$$T_e = \frac{3}{2}\frac{p}{2}\Psi_m i_{sq}\text{[AC Machines,2008]} \tag{2.21}$$

Power Equations The expression of the active and reactive power are presented in Eq.2.22, respectively Eq.2.23.

$$P = u_{sd} i_{sd} + u_{sq} i_{sq} \tag{2.22}$$

$$Q = u_{sd} i_{sq} - u_{sq} i_{sd} \tag{2.23}$$

The general mechanical equation of the machine is:

$$T_e = T_L + B\omega_m + T_d + J\frac{d}{dt}\omega_m \tag{2.24}$$

where:

T_L - load torque

B - viscous friction

T_d - dry friction torque

J - moment of inertia

2.4.2 Simulation results

The equations described in the previuos section are implemented in Matlab/Simulink. The simulation blocks are presented in Appendix D. For the simulation the parameters presented in Table2.1 were used.

The voltages for the nominal working point of the machine ($n = 1750[rpm]; T_L = 12[Nm]$), are presented in Fig.2.7. The machine is run at no load and rated speed, and at time 0.5[sec] the rated load torque is applied.

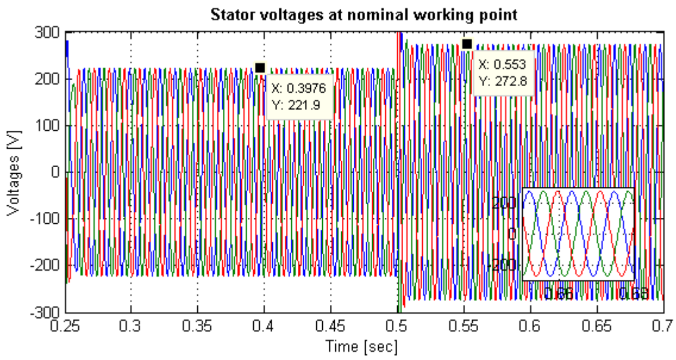

Figure 2.7: *Stator phase voltages at nominal working point*

As it can be seen in Fig.2.7, the no load voltages have a smaller amplitude that at rated torque. At the nominal load torque, the voltage amplitude is 272[V], which is close to the expected value $U = 285[V]$. A zoom in the figure is made, to show that the voltages are sinusoidal.

In Fig.2.8, the stator currents for the nominal working point are shown. At no load, the currents are 0, and at rated load torque the current amplitude is approximately 6.6[A] which is close to the expected value $I = 6.1[A]$

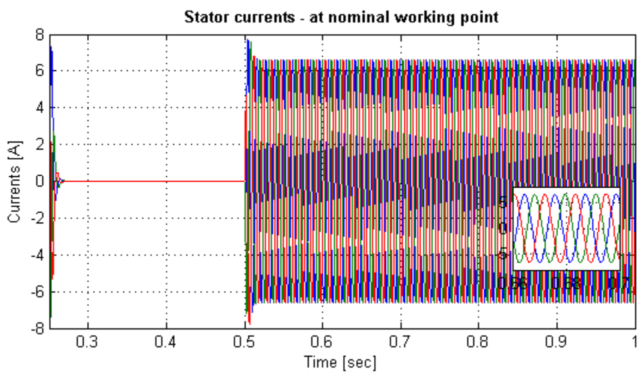

Figure 2.8: *Stator phase currents at nominal working point*

Conclusions

In this chapter a description of the general system was presented. The Space Vector Modulation strategy for the converter control was introduced and the validation of the simulation was presented. The model of the PMSM was build in order to be used in the simulation of the machine control.

3
Field Oriented Control

In this chapter the control strategy for the PMSG is introduced. First an introduction to Field Oriented Control is presented. In the next section, the current and speed controllers design and performances are described. The Field Oriented Control method is tested in Matlab/Simulink and the results are presented.

3.1 Introduction to Field Oriented Control(FOC)

The variable speed wind turbines are becoming the most attractive solution, due to the fact that, at variable speed, maximum power can be extracted. But the amount of energy obtained from a wind turbine depends not only on the wind regime at the site, but also on the control strategy used for the wind turbine. A popular technique for control of the PMSG is Field Oriented Control, which uses the rotor position and speed of the generator.

FOC is a closed loop control structure, where the torque is controlled indirectly, by controlling the stator current. The control strategy is expressed in the dq reference frame. The torque expression in the dq system of coordinates, for the surface mounted PMSG, is presented in the Eq.3.1.

$$T_e = \frac{3}{2}\frac{p}{2}\Psi_m i_{sq} \tag{3.1}$$

Even though the control in this project is implemented on a PM synchronous machine which presents some saliency, $\zeta = L_q/L_d = 1.2$, this is neglected for simplicity. As the Eq.3.1 shows, with Ψ_m constant, by controlling the q- axis stator current, the torque can be controlled.

The torque can be controlled by keeping the torque angle as desired. There are several ways to control the torque:

- Constant angle control - for this control α-the torque angle is kept at 90^o. The d-axis current component is set to be 0, which makes the stator current to have only the q-axis component. Since the permanent magnet flux and the torque angle are constant, the torque depends only on the q-axis component of the stator current amplitude.

- Maximum torque per ampere control - for the surface mounted PMSG this method is the same as the constant angle control (for $\alpha = \frac{\pi}{2}$).

- Unity power factor control

- Constant stator flux control - for this the amplitude of the stator flux vector is kept constant and equal to the permanent magnet flux vector.

Considering that the focus in this project is not to implement an optimum control strategy, but to implement a sensorless control, the constant angle control is chosen for simplicity.

In Fig.3.1 a space vector diagram of the control is presented. The torque is kept as desired by controlling the current vector. The permanent magnet flux is aligned with the d-axis.

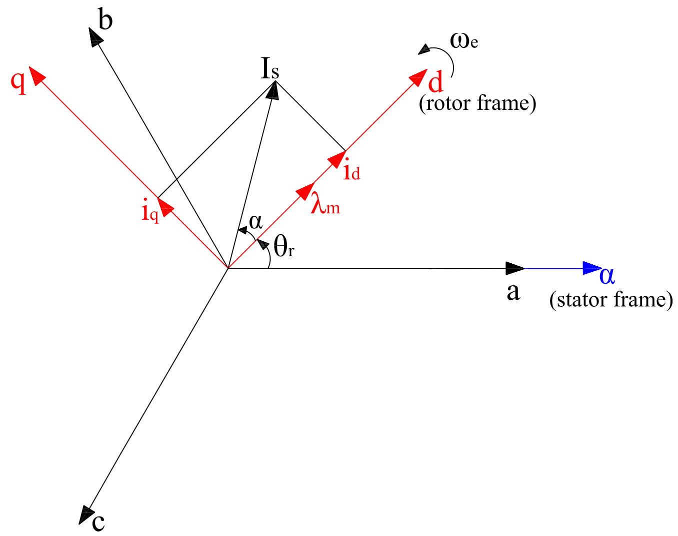

Figure 3.1: *Field Oriented Control phasor diagram*

In the figure α is the torque angle, θ_r is the load angle and $I_s = i_{sd} + ji_{sq}$ is the stator current vector.

The structure of the control algorithm is presented in Fig.3.2.

The measured parameters for this control are the DC voltage, the stator currents and the rotor position. In this chapter the rotor position is determined considering that an encoder is mounted on the rotor. The i_{sd} reference current is set to be 0 and i_{sq} reference current is given by the PI (Proportional Integral) speed controller. The required dq voltages are obtained from 2 PI current controllers. In order to control the currents independent one of each other, the compensation terms, $\omega_e\Psi_d$ is added, and $\omega_e\Psi_q$ is subtracted, at the output of the PI current controllers. Space Vector Modulation is used to create the duty cycles for the desired reference voltages and PWM generator block calculates the switching signals for the power converter.

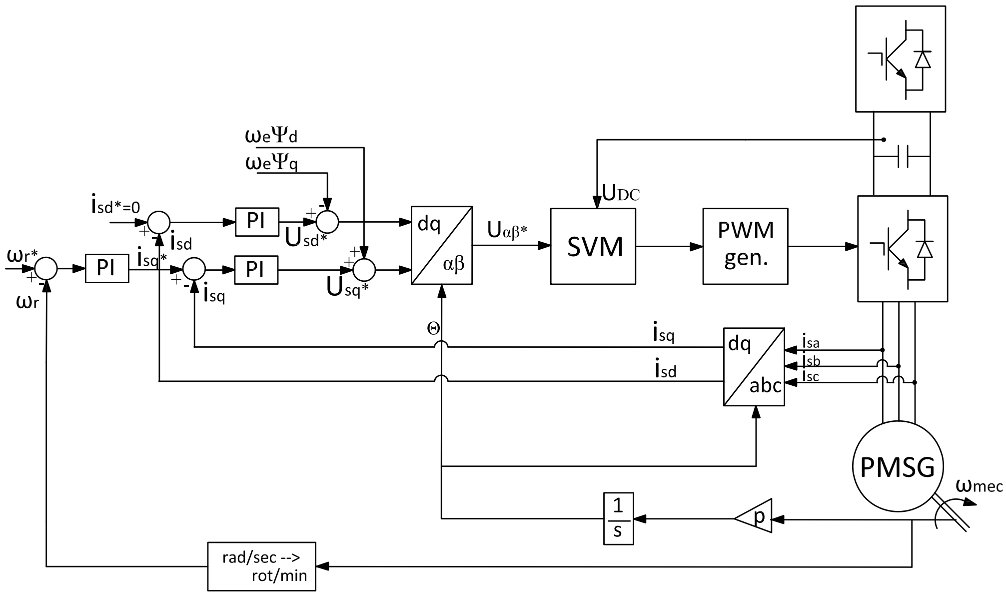

Figure 3.2: *Field Oriented Control scheme with sensor*

3.2 Current and speed controllers design

In this section, the implementation of the currents and the speed controllers is presented. The overall structure of the q and d-axis control loops is presented in Fig.3.3.

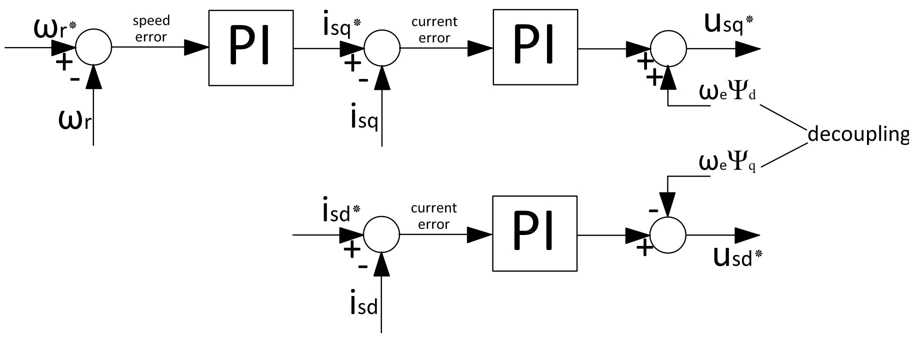

Figure 3.3: *q- and d- axis control loop structure*

where,

ω_r - electrical speed in rot/min;

ω_e - electrical speed in rad/sec.

In Fig.3.3, for the q-axis, the speed loop is the outer loop and the current loop is the inner one. The error, between the reference speed ω_r^* and the measured speed ω_r, is the input to a proportional integral (PI) speed controller. At the output, the reference signal i_{sq}^* is generated. The errors between the reference currents $i_{sq,d}^*$ and the measured currents

$i_{sq,d}$ are the input to other 2 PI controllers (current controllers), in order to generate the reference voltage $u_{sq,d}$, applied to the motor. The decoupling factor was derived from the stator voltage equations in dq reference frame.

$$u_{sq} = R_s i_{sq} + \frac{d\Psi_q}{dt} + \omega_e \Psi_d \tag{3.2}$$

$$u_{sd} = R_s i_{sd} + \frac{d\Psi_d}{dt} - \omega_e \Psi_q \tag{3.3}$$

The common term of the two voltage equations is the back-emf. So, by subtracting the back-emf term, in the current controller part, the two currents i_{sd} and i_{sq} will be independent of each other. This also makes it easier for the tuning of the PI current controllers because it simplifies the transfer function of the motor.

In the followings the current and speed controllers are presented.

3.2.1 q-axis current controller

First the i_{sq} current controller is designed. The i_{sq} loop is presented in Fig.3.4.

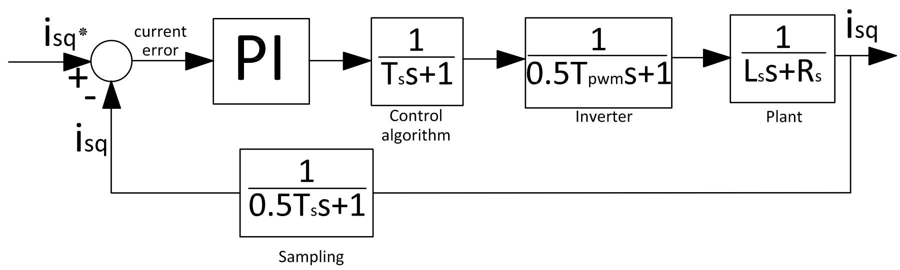

Figure 3.4: *q-axis current control loop structure*

The blocks in the figure are:

- The PI current controller
- The delay introduced by the digital calculation. This has the form of a first order transfer function with the time constant $T_s = \frac{1}{f_s} = 0.2[ms]$, where $f_s = 5[kHz]$ is the sampling frequency.
- The delay introduced by the PWM inverter, which is considered as first order transfer function with the time constant $0.5T_{PWM} = \frac{1}{f_{PWM}=0.1[ms]}$, where f_{PWM} is the switching frequency.
- The plant block.
- The delay introduced for the digital to analog conversion. This has also the form of a first order transfer function with the time constant $0.5T_s = 0.1[ms]$.

The transfer function of the PI controller is [Kazmierkowski,1995]:

$$PI_{i_q} = k_{pi_q}(1 + \frac{1}{T_{i_q}s}) = k_{pi_q}\frac{1 + T_{i_q}s}{T_{i_q}s} \tag{3.4}$$

where,

k_{pi_q} - proportional gain of the q-axis current controller;

T_{i_q} - integral time of the q-axis current controller.

The transfer function of the plant is presented in Eq.3.5.

$$\frac{i_{sq}}{v_{sq}} = \frac{1}{R_s + sL_q} = \frac{1}{R_s}\frac{1}{1 + s\frac{L_q}{R_s}} = \frac{K}{1 + s \cdot \tau_q} \tag{3.5}$$

where,

$$K = \frac{1}{R_s} \tag{3.6}$$

$$\tau_q = \frac{L_q}{R_s} = 0.0201[sec] \tag{3.7}$$

The feedback path, in Fig.3.4, can be moved on the forward path as in Fig.3.5.

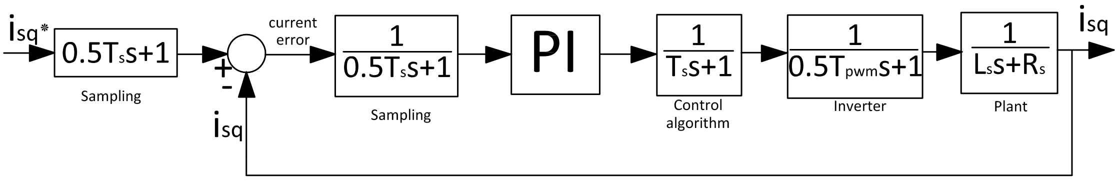

Figure 3.5: *q-axis current control loop structure with unity feedback*

The open loop transfer function is represented by the Eq.3.8:

$$G_{i_q}(s) = k_{pi_q}\frac{1 + T_{i_q}s}{T_{i_q}s}\frac{K}{\tau_q s + 1}\frac{1}{T_s s + 1}\frac{1}{0.5T_s s + 1}\frac{1}{0.5T_{pwm}s + 1} \tag{3.8}$$

The zero of the controller is used to cancel the slowest pole of the transfer function, which is the machine pole. This means that $T_{i_q} = \tau_q = 20[ms]$. In Fig.3.6 the root locus of the designed q-axis current controller is presented.

In order to simplify the transfer function, an equivalent time constant can be defined,

$$T_{si} = 1.5T_s + T_{pwm} = 0.3 + 0.1 = 0.4[ms] \tag{3.9}$$

and the open loop transfer function becomes:

$$G_{i_q}(s) = k_{pi_q}\frac{1}{T_{i_q}s}K\frac{1}{T_{si}s + 1} \tag{3.10}$$

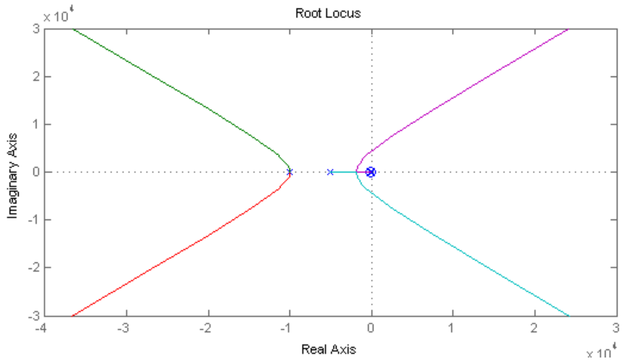

Figure 3.6: *Root locus of the q-axis current controller*

The proportional gain of the PI controller, k_{pi_q}, is calculated using the optimal modulus(OM) criterion, with the damping factor set to be $\zeta = \frac{\sqrt{(2)}}{2}$.[Kazmierkowski,1995]. The standard transfer of a second order system is presented in Eq.3.11:

$$G_{OM} = \frac{1}{2\tau s(\tau s + 1)} \tag{3.11}$$

Making the analogy between the Eq.3.10 and the Eq.3.11, it results:

$$\frac{k_{pi_q} K}{T_{i_q}} = \frac{1}{2T_{si}} \tag{3.12}$$

and

$$k_{pi_q} = \frac{T_{iq} R_s}{2T_{si}} = 47.87 \tag{3.13}$$

The Bode diagram of designed current controller is presented in Fig.3.7.

The implemented design of the I_{sq} PI controller leads to a gain margin of GM=15.2(dB) and a phase margin, PM=62,9(deg) (see Fig3.7). As it can be seen in the figure the closed loop system is stable.

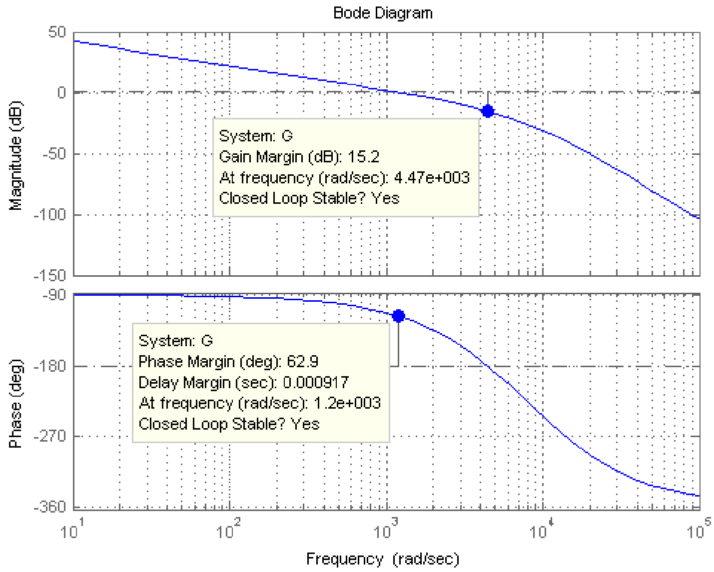

Figure 3.7: *Bode diagram of the q-axis current controller*

Previously the q-axis current controller was designed in s-domain. In order to be able to implement the control in real time, the controllers are implemented also in z domain. The transfer function of the PI current controller in z domain is presented in Eq.3.14.

$$PI_{iq}(z) = 48.11 + \frac{0.48}{z-1} \tag{3.14}$$

Figure 3.8 presents the step response of the designed q-axis current controller. In Fig.3.8(a)

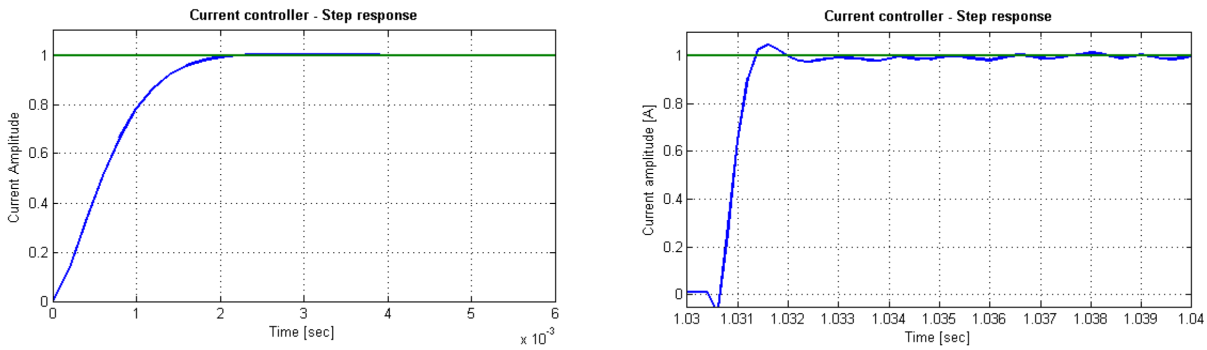

Figure 3.8: *Step response of the q-axis current controller: (a) Simulation results (b) Laboratory results*

the step response of the controller in z domain is presented. It can be seen in the figure, that the settling time of the controller is $t_s = 4[ms]$ and no overshoot occurs while reaching steady state. For validation, the q-axis current controller is tested also in laboratory. For the test, the reference value for the d-axis current is kept zero and the reference value for the q-axis current is a step of 1A. As it can be seen in Fig.3.8, the implemented controller in the laboratory has a good response: a very small overshoot 4% and a settling time comparable to the one in the simulation.

3.2.2 q-axis speed controller

The speed loop is presented in Fig.3.9.

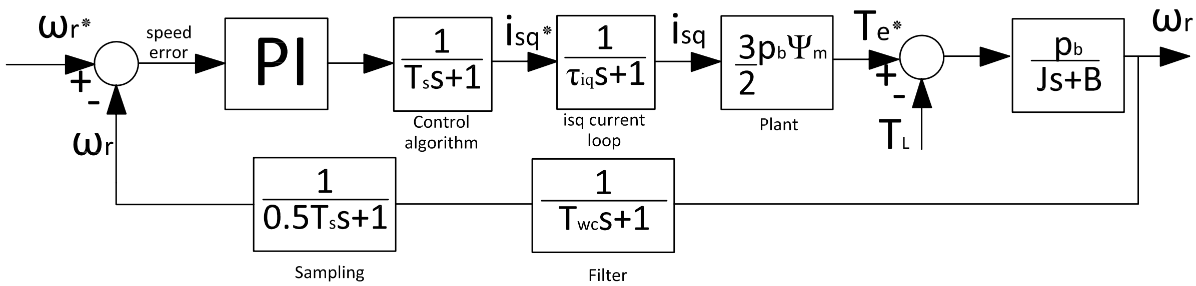

Figure 3.9: *q-axis speed control loop*

where,

T_e - electromagnetic torque;

T_L - load torque;

p_b - number of pair poles;

ω_r - mechanical speed in rpm.

In the figure, the blocks are:

- The PI speed controller.
- The delay introduced by the digital calculation. This has the form of a first order transfer function with the time constant $T_s = \frac{1}{f_s} = 0.2[ms]$, where $f_s = 5[kHz]$ is the sampling frequency.
- The delay introduced by the current controller.
- The plant.
- The delay introduced for the digital to analog conversion. This has also the form of a first order transfer function with the time constant $0.5T_s = 0.1[ms]$.
- For the sensored control, the speed is measured with an encoder mounted on the shaft of the machine. The measured speed needs to be filtered. The filter has the cut-off frequency of 200[Hz] which means $\omega_c = 2\pi f = 1256[rad/sec]$. The time constant of the filter is $T_{\omega_c} = \frac{1}{\omega_c} = 0.796[ms]$

The transfer function of the PI speed controller is:

$$PI_\omega = k_{p\omega}(1 + \frac{1}{T_\omega s}) = k_{p_\omega}\frac{1 + T_\omega s}{T_\omega s} \tag{3.15}$$

where,

$k_{p\omega}$ - proportional gain of the speed controller;

T_ω - integral time of the speed controller.

The current controller can be modeled as a first order function with the transfer function presented in Eq.3.16.

$$G_{iq}(s) = \frac{1}{1 + \tau_{iq}s} \tag{3.16}$$

where, $\tau_{iq} = \frac{T_{iq}}{k_{piq}K} = 0.798[ms]$

The electrical speed of the generator is calculated from the mechanical equation.

$$T_e - T_L = \frac{J}{p_b}\frac{d}{dt}\omega_m + \frac{B}{p_b}\omega_m \tag{3.17}$$

where,

$$T_e = \frac{3}{2}p_b\Psi_m i_{sq} \tag{3.18}$$

As the viscous friction coefficient is very small, it is possible to omit it when designing the speed PI controller. The electrical speed becomes:

$$\omega_m = \frac{p_b}{Js}(T_e - T_L) \tag{3.19}$$

As performed for the current controller, the feedback path in Fig.3.9 can be moved in the forward path and without the disturbance the system looks like in the Fig.3.10. The open

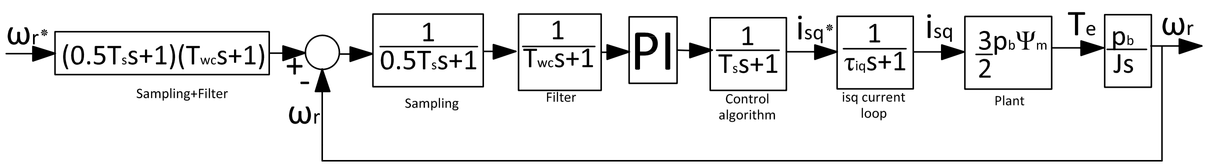

Figure 3.10: *q-axis speed control loop structure with unity feedback and without disturbance*

loop transfer function is presented in Eq.3.20.

$$G_\omega(s) = \frac{1}{0.5T_s + 1}\frac{1}{T_{\omega_c}s + 1}k_{p\omega}\frac{T_\omega s + 1}{T_\omega s}\frac{1}{T_s + 1}\frac{1}{\tau_{iq}s + 1}\frac{3}{2}p_b\Psi_m\frac{p_b}{Js} \tag{3.20}$$

In order to simplify the transfer function, an equivalent time constant can be defined,

$$T_{s\omega} = 1.5T_s + \tau_{iq} + T_{\omega_c} = 0.3 + 0.798 + 0.796 = 1.894[ms] \tag{3.21}$$

If $K_T = \frac{3}{2} p_b \Psi_m$ the open loop transfer function becomes:

$$G_\omega(s) = \frac{p_b K_T K_{p\omega}(T_\omega s + 1)}{J T_\omega s^2 (T\omega s + 1)} \tag{3.22}$$

The load torque is a disturbance from the point of view of the controller. The optimal response to the disturbance is obtained tuning the regulator according to the Optimum Symmetric Method(OSM). [Mizera,2005] The standard form of the open loop transfer function of the Optimum Symmetric Method is:

$$G_{OSM}(s) = \frac{K_1 K_p T_I s + K_1 K_p}{s^2(T_1 T_I s + T_I)} \tag{3.23}$$

The speed transfer function is modeled as to be similar to the standard transfer function of the OSM:

$$G_\omega(s) = \frac{\frac{p_b K_T}{J} k_{p\omega} T_\omega s + \frac{p_b K_T}{J} k_{p\omega}}{s^2(T_{s\omega} T_\omega s + T_\omega)} \tag{3.24}$$

Based on Eq.3.23 and Eq.3.24, using the optimum symmetric method, [Mizera,2005], the proportional and the integral gain of the speed controller are obtained.

$$k_{p\omega} = \frac{1}{2K_1 T_1} = \frac{1}{2p_b \frac{K_T}{J} T_{s\omega}} = 0.927 \tag{3.25}$$

$$T_\omega = 4T_1 = 4T_{s\omega} = 7.6[ms] \tag{3.26}$$

The Bode diagram is presented in Fig.3.11.

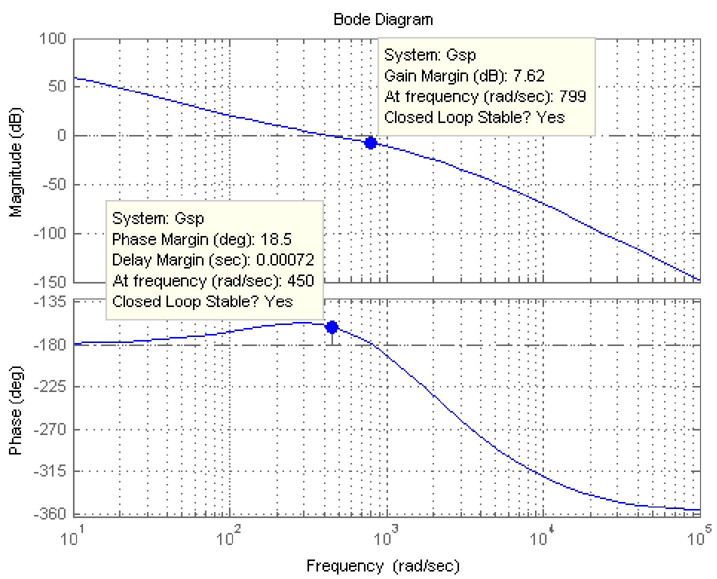

Figure 3.11: *Bode diagram of the speed controller*

The implemented design of the speed PI controller leads to a gain margin of GM=7.62(dB) and a phase margin, PM=18.5(deg) (see Fig3.11). The closed loop system is stable.

As presented for the current controller, the speed controller is also implemented in z domain. Equation 3.27 presents the transfer function of the PI speed controller in z domain.

$$PI_{\omega}(z) = 0.9211 + \frac{0.0243}{z-1} \tag{3.27}$$

The step response of the speed controller, presented in Fig.3.12(a), is characterized by:

- Overshoot $M_{p\%} \approx 76\%$
- Settling time $t_s \approx 0.07[sec]$

The overshoot of the speed controller is very big, which means that in the control system it will cause a very high starting q current. To overcome this, the current is limited and an antiwindup circuit for the PI controller is used. This will result in a smaller overshoot in the speed response. The designed controller is implemented in the control structure in the laboratory. In Fig.3.12 (b), a step of 500[rpm] is applied to the machine, and the speed response is presented. The speed response of the machine presents an overshoot of

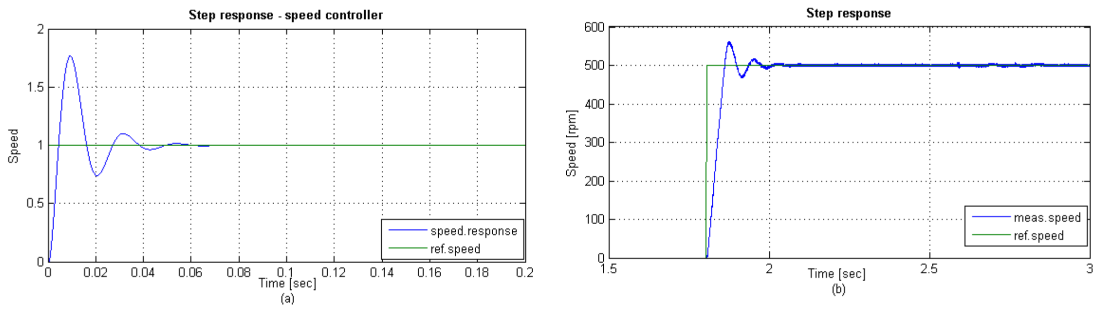

Figure 3.12: *Speed step response: (a) Step response of the q-axis speed controller (b) Speed response to a 500[rpm] step*

$M_p = 12\%$, and has a settling time of $t_s = 0.24[sec]$, which are acceptable performances in the real system. As observed before, the overshoot is smaller due to the antiwindup circuit.

3.2.3 d-axis speed controller

The d-axis current controller is implemented in the same way as the q-axis current controller.

The transfer function of the plant is presented in Eq.3.28.

$$\frac{i_{sd}}{v_{sd}} = \frac{1}{R_s + sL_d} = \frac{1}{R_s}\frac{1}{1+s\frac{L_d}{R_s}} = \frac{K}{1+s\cdot\tau_d} \tag{3.28}$$

where,

$$K = \frac{1}{R_s} \tag{3.29}$$

$$\tau_d = \frac{L_{sd}}{R_s} = 0.015[sec] \tag{3.30}$$

The integral time of the d-axis current controller is $T_{id} = \tau_d = 15[ms]$.

The proportional gain of the d-axis current controller is $k_{pi_d} = \frac{T_{id}R}{2T_{si}} = 37.87$.

In Fig.3.13 the Bode diagram of the I_d current loop is presented. It has a gain margin $G_M = 17.2(db)$ and a phase margin $PM = 67.3(deg)$. As the figure shows the system is stable.

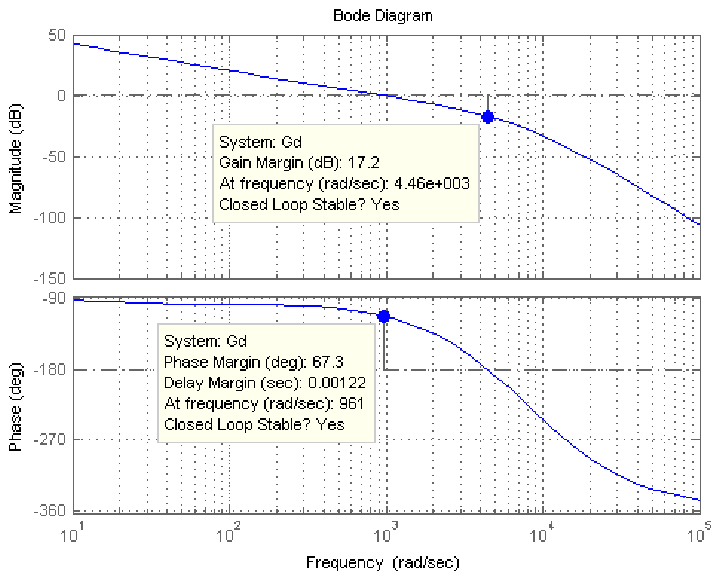

Figure 3.13: *Bode diagram of the d-axis current controller*

The transfer function of the PI current controller in z domain is as shown in Eq.3.31.

$$PI_{iq}(z) = 38.11 + \frac{0.47}{z-1} \tag{3.31}$$

Figure 3.14 presents the step response of the designed q-axis current controller in z domain.

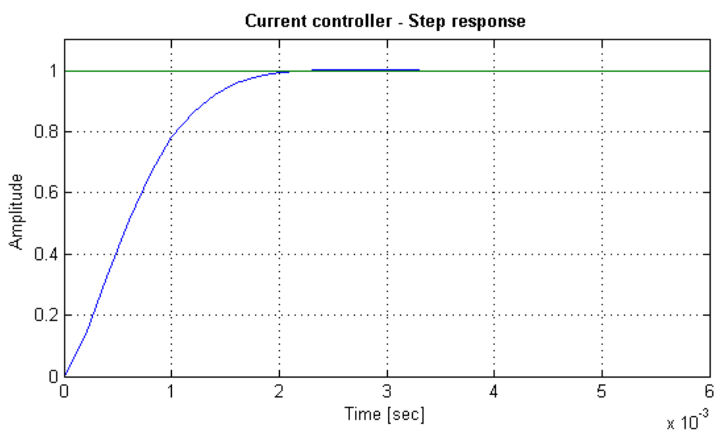

Figure 3.14: *Step response of the d-axis current controller*

As it can be seen in the figure, the step response has a settling time of approximately $t_s = 3.5[ms]$ and presents a very small overshoot.

3.3 Antiwindup

The output signals (current and voltage) of the designed controllers, need to be limited in order not to exceed their maximum value. This means that saturation can occur if the limit is reached. When saturation happens, the control signal is not changing anymore which makes the feedback path to be opened. In this case, if the error is still applied to the input of the integrator, its output will continuously grow, until the sign of the error changes and the integration turns around. The effects of this phenomenon are that the output can have a large overshoot and poor transient response. [Franklin,2006] In order to solve this problem an integrator antiwindup circuit, which turns off the integral action when the actuator saturates, is used. The antiwindup scheme is presented in Fig.3.15. One effect of the antiwindup is

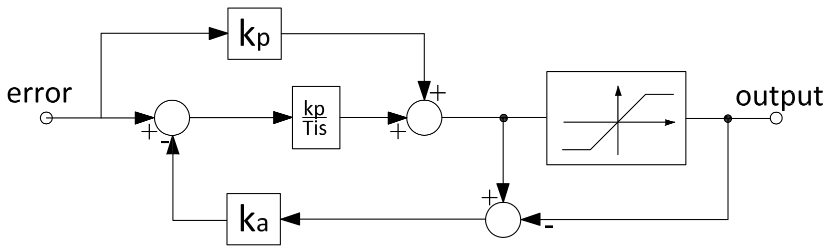

Figure 3.15: *Integrator antiwindup scheme [Franklin,2006]*

to reduce the overshoot. When the saturation occurs, the antiwindup gain has to be large enough so that the input to the integrator to be as small as possible. The chosen value for the antiwindup gain of the speed controller is $k_a = 10$ and of the current controllers is $k_a = 0.1$.

3.4 Simulations results

Having the controllers working properly, the Field Oriented Control needs to be tested. In order to be able to implement the control further, in laboratory, the simulation is designed in discrete domain. The sampling frequency used is $f_s = 5[kHz]$. The Simulink blocks of the control are presented in Appendix D. In the simulation, the Space Vector Modulation block, for the duty cycles generation, was taken from dSpace laboratory, IET. In this section the simulation results of the implemented control are presented. The control is tested for different conditions: steps in speed, steps in load, motor and generator operation.

3.4.1 Motor operation at no load, 50% rated speed, step to rated speed

For this test the machine is run at no load, at 50% rated speed ($n = 875[rpm]$). A step to the rated speed ($n = 1750[rpm]$) is applied at 1[sec]. The following results are showing the behavior of the simulated model.

In Fig.3.16 (a) and (b) the stator voltages and currents, for the presented conditions, are shown. It can be seen in the zoom made on the voltages that the signals are sinusoidal. The voltage amplitude, at no load and 50% rated speed is 111[V] and at rated speed is 222[V]. As expected, in the simulations, the value of the currents at no load is zero (Fig.3.16 (b)). In transients, when the motor accelerates to the rated speed, the currents are limited to 7.6[A] which is 1.25 times their rated value.

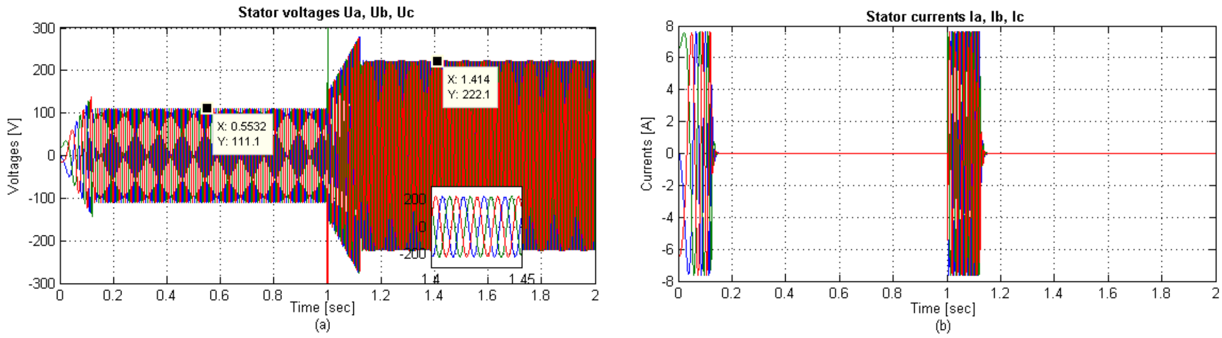

Figure 3.16: *Stator voltages and currents at no load and rated speed, speed step to nominal speed (a) Measured voltages (b) Measured currents*

In Fig.3.17 the speed step response is presented. It can be seen in the figure, that the measured speed is following with good accuracy the reference. The speed stabilizes with no overshoot at approximately 0.15[sec]. The reason why there is no overshoot and the speed stabilizes slower than when the speed controller was tested, is due to the integrator antiwindup circuit.

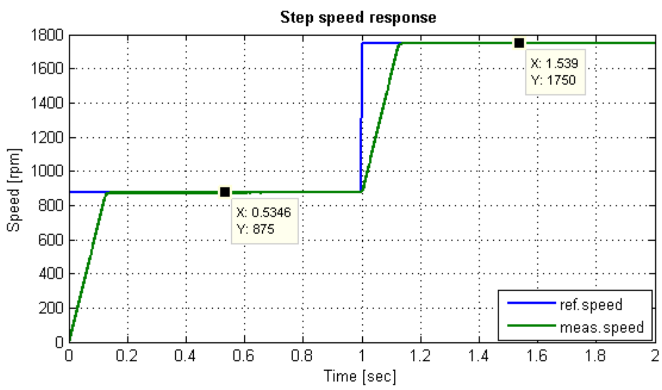

Figure 3.17: *Speed response to a step of 50% rated speed and a step to the rated speed*

3.4.2 Motor operation at 50% rated speed, 50% load torque, step in speed to rated speed, step in load to rated torque

For this test the machine is run in motor mode at 50% rated speed ($n = 875[rpm]$) and no load. At 0.5[sec], a step of 50% rated torque ($T_L = 6[Nm]$) is applied. A step of speed to rated speed is applied at 1[sec] and another step in load to rated load torque is applied after 2[sec]. The results of the simulations are presented next.

In Fig.3.18(a) and (b), the measured voltage and current responses to the presented conditions are shown.

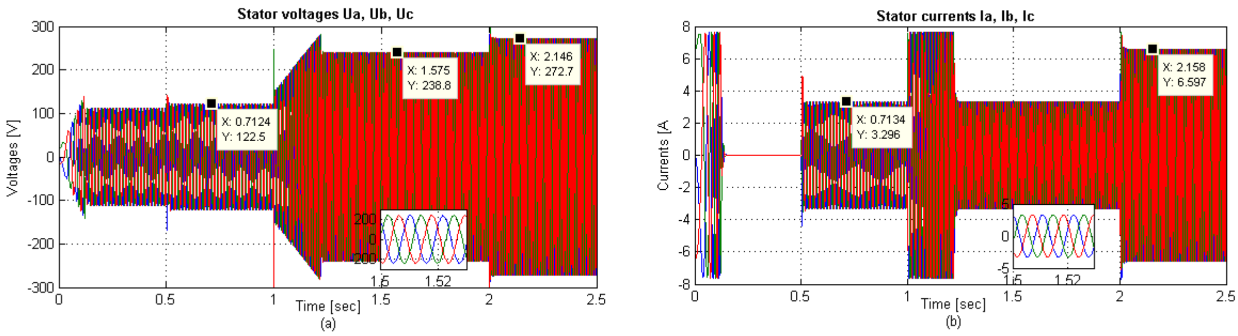

Figure 3.18: *Stator voltages and currents at different conditions: (a) Measured voltages (b) Measured currents*

From Fig.3.18 (a) the amplitude of the voltages can be read. It can be seen that, at rated speed and rated torque, the amplitude of the voltages is approximately 273[V], which is close to the expected ones 285[V].

From the electromagnetic torque expression, Eq.3.1, the rated q axis current can be calculated. Having the d-axis current kept to zero by the control strategy (see Fig.3.19 (a)), the amplitude of the current vector is equal to the magnitude of the q axis current, which is calculated to be 6.7[A]. As shown in Fig.3.18 (b) at nominal rated torque the value of the currents is 3.29[A] and at rated torque the currents value is 6.59[A], as expected. Also, it can be seen in the zoom performed in both figures that the signals are sinusoidal.

The I_{sd} and I_{sq} reference and measured values are presented in Fig.3.19. As shown in

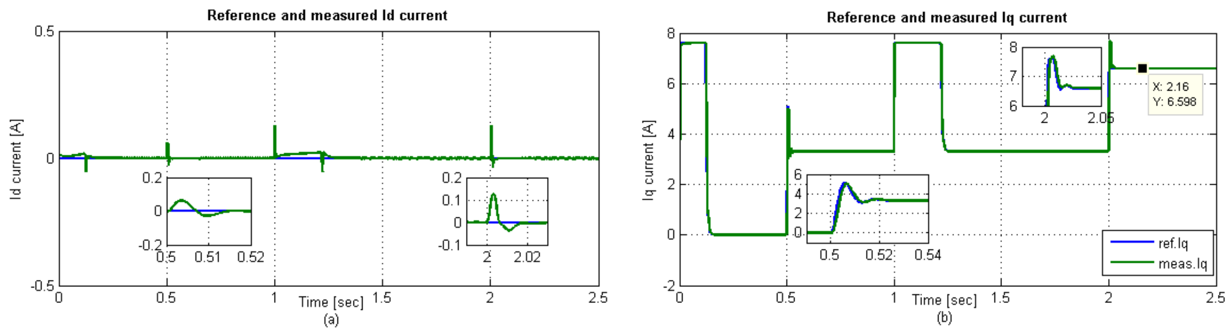

Figure 3.19: *Measured and reference currents: (a) d-axis current (b) q-axis current*

Fig.3.19 (a) and (b), the measured currents are following with good accuracy the references.

The value of the d-current is 0 and the value of the q-current at rated torque is 6.59[A], as expected. In the zooms made in Fig.3.19 (a) and (b), the response of the currents can be seen. The settling time is small and when the load torque is applied, small overshoots appear in i_d current. In Fig.3.20, the electromagnetic torque and the machine speed are shown.

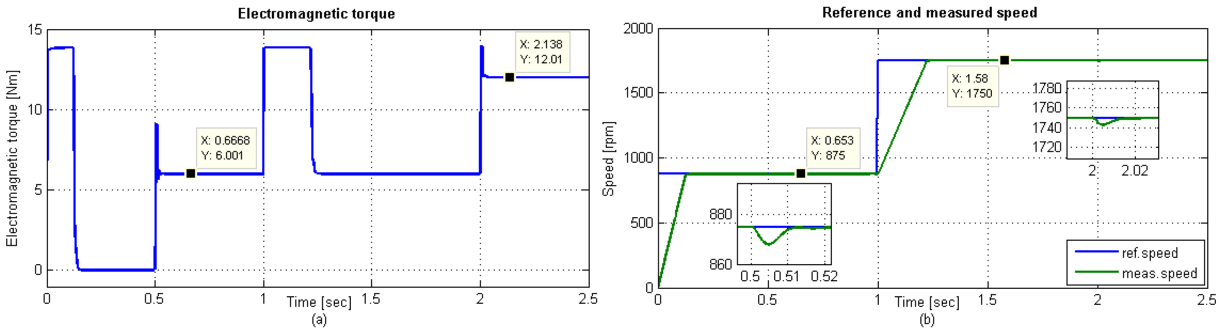

Figure 3.20: *Response to different conditions: (a) Electromagnetic torque (b) Machine speed*

It can be seen in Fig.3.20 (a) that the torque is saturated, in transients, when the currents are limited. Also an overshoot appears when the step load torque is applied. In Fig.3.20 (b), the speed follows with good accuracy the reference. No overshoot appears when the speed reaches the rated value, but a small backward overshoot appears when the torque is applied at 0.5[sec] and 2[sec] (as shown in the zooms in Fig.3.20 (b)). It can also be seen that the settling time is slower (0.24[sec]), when the speed step is applied to the loaded machine, than the settling time when the machine is unloaded (0.15[sec]).

3.4.3 Motor and Generator operation at rated speed ($n = 1750[rpm]$ and rated torque ($T_L = 12[Nm]$)

. The motor and generator modes of the machine are presented in the following simulations. For this test the machine was run at no load at the rated speed). At 0.5[sec], the machine is run in motor mode at nominal load torque and after 1[sec] in generator mode. In Fig.3.21 the electromagnetic torque and the electric power are shown. As it can be seen in the figure, the torque is positive for the motor operation and negative for the generator mode. The same applies to the electrical power.

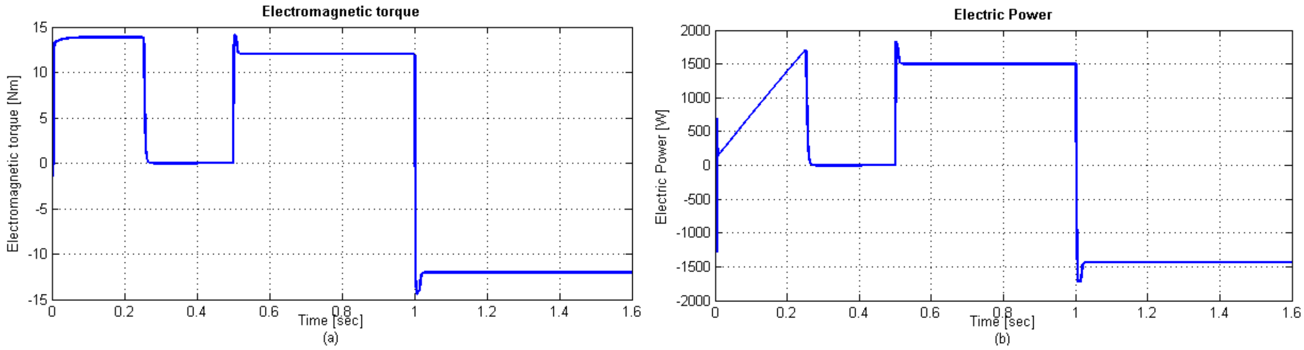

Figure 3.21: *Motor and generator operation at nominal load torque: (a) Electromagnetic torque (b) Electric Power*

The speed response to the presented conditions, is presented in Fig.3.22.

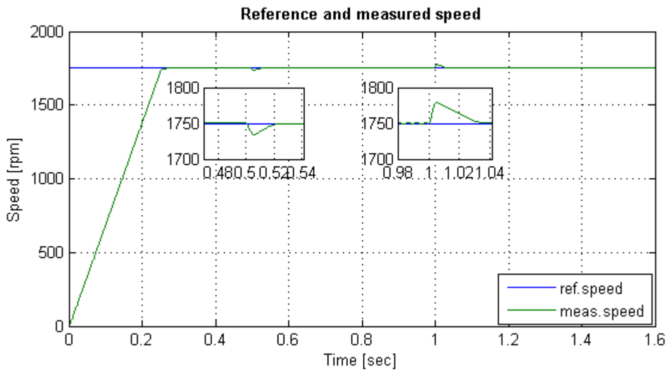

Figure 3.22: *Speed response in motor and generator operation of the machine*

As shown in the figure, the measured speed is following the reference speed. Zooms are made in the figure, in order to see the speed response when the load torques are applied. This test shows that the designed control is working properly also for generator operation of the machine.

Conclusions

In this chapter the field oriented control was introduced. The controllers were designed and their performances were presented. As the controllers showed satisfactory responses, the field oriented control was tested. The presented results show that the control is working properly and it can be tested in real time in laboratory.

4
Sensorless Control

In this chapter the algorithm for the rotor position and speed estimations is presented. At the beginning, an introduction to sensorless control is presented and methods for rotor position estimation are introduced. The chosen method is further described. Results of the simulations and conclusions are presented at the end of the chapter.

4.1 Introduction to Sensorless Control

In the previous chapter the Field Oriented Control strategy was introduced. The position and the speed were determined from measurements considering position sensor installed on the rotor. But using a sensor has several drawbacks, like the increased cost, size and reliability of the drive system. Therefore, it is an increased interest in eliminating the rotor mounted mechanical sensor.

The Field Oriented Control scheme with the position and speed estimations is presented in Fig.4.1.

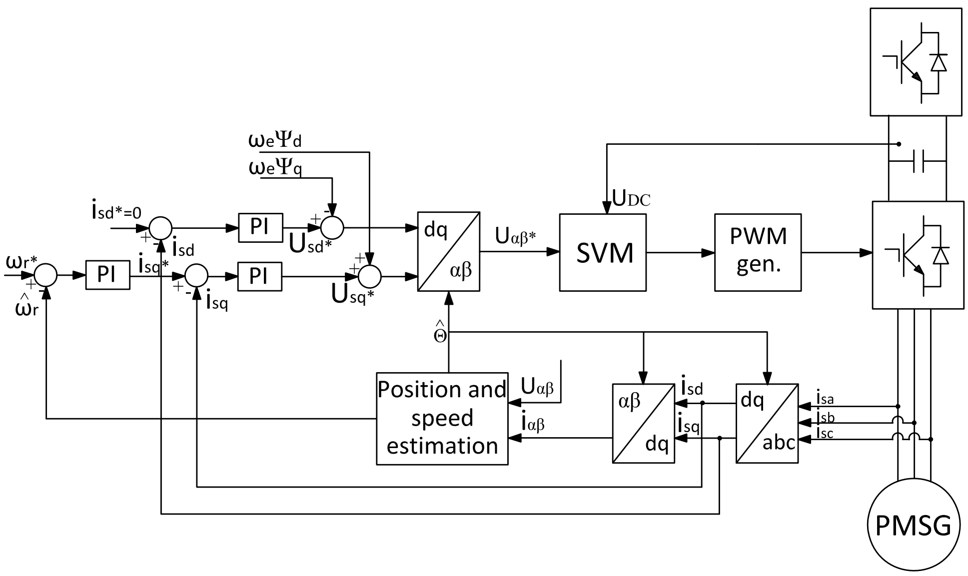

Figure 4.1: *Field Oriented Control scheme without sensor*

Many methods for detecting the rotor position are presented in literature. Most of the methods have been developed for the IPMSM (interior permanent magnet synchronous machine), because of the inductance variation in the d- and q- axis, which makes the rotor position easier to monitor. For surface mounted permanent magnet synchronous machine it is more difficult to control the speed more accurately, especially at zero and very low speeds. The difficulty with the surface mounted rotor is that the d- and q- axis inductances are equal. But the advantages, like lower costs and simpler mechanical structure, of the SMPMSM makes the research for sensorless control for this kind of machine to be significant. [Song,2006]

- One of the methods used for monitoring the rotor position is based on the back-emf calculation. The idea of this method is to compute the back-emf vector in order to get the rotor position angle.

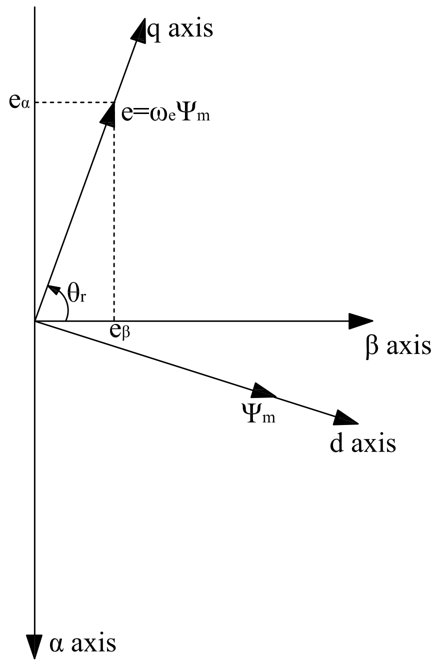

Figure 4.2: *Back-EMF vectorial representation in the stationary reference frame.*

As it can be seen in Fig.4.2 the permanent magnet flux(Ψ_m) is aligned with the d-axis, therefore the back-EMF vector is aligned with the q-axis and indicate the rotor position angle θ_r. Using the voltage equations, the α and β components of the back-emf are presented in the following equations.

$$e_\alpha = \omega_e \Psi_m sin(\theta_r) = -u_\alpha + R_s i_\alpha + L\frac{d}{dt}i_\alpha \tag{4.1}$$

$$e_\beta = \omega_e \Psi_m cos(\theta_r) = u_\beta - R_s i_\beta - L\frac{d}{dt}i_\beta \tag{4.2}$$

Then the rotor position is calculated using Eq.4.3.

$$\theta_r = tan^{-1}\frac{e_\alpha}{e_\beta} \tag{4.3}$$

The main problem with this method is the position estimation at zero speed and at low speeds. In Eq.4.1 and Eq.4.2 it can be seen that at zero speed the back-emf components become zero, which means that the position monitoring is not possible. At low speeds the back-emf is small and the noise leads to a large error in the position estimation. Other errors, in the back-emf estimation, can be introduced also by the differentiation term of the currents.

- Another common method for estimating the rotor position is based on injection of a high frequency signal. This method can estimate the position also at zero and low speeds, but is more suitable for the IPMSM because this kind of machine presents saliency. Also this method is not suitable for direct driven wind turbines (as in the present case), where the switching frequency is low.

- Another method for position estimation is based on the flux linkage estimation. The flux linkages can be estimated from the stationary reference frame voltage equations, Eq.4.4 and Eq.4.5.

$$\Psi_\alpha = \int (u_\alpha - R_s i_\alpha) dt \tag{4.4}$$

$$\Psi_\beta = \int (u_\beta - R_s i_\beta) dt \tag{4.5}$$

  As it can be seen in the equations, the phase voltages, currents and the stator resistance need to be known to estimate the fluxes. One of the problems introduced by this method is the integration drift, which can be avoided by using proper integration techniques. Also the initial position of the rotor can not be estimated with this technique.

- Another method for monitoring the rotor position is using observers based on the motor model. The purpose of the state observer is that, using the same inputs as the one used to drive the machine, the dynamics of the machine are modeled to control that the states (rotor position, velocity) of the modeled machine are the same as the real one. The observer uses the error, between the measured values (from the machines outputs) and the modeled ones, to correct the estimations of the different states.

  In [Brahmi,2008] a model reference adaptive observer (MRAS) is implemented. The estimator uses two models to calculate the flux of the PMSG. The reference model, consists of the stator flux equations and the adaptive model, which considers the rotor speed as the adjustable parameter, is shown in the following equations:

$$\hat{\Psi}_{sd} = \int (U_{sd} + \hat{\omega} L \hat{I}_{sq} - R_s \hat{I}_{sd}) dt + \Psi_m \tag{4.6}$$

$$\hat{\Psi}_{sq} = \int (U_{sq} - \hat{\omega} L \hat{I}_{sd} - R_s \hat{I}_{sq} - \hat{\omega} \Psi_m) dt \tag{4.7}$$

  The block diagram of the control is presented in Fig.4.3.

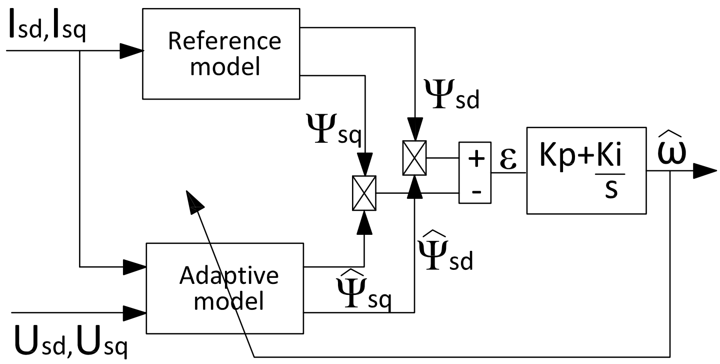

Figure 4.3: *Block diagram for MRAS control*

The adjustable parameter (the speed) tunes the adaptive model in order to drive the output error between the two models to zero. The error of the two models is the input to a PI controller, which is used to tune the speed such that the error becomes zero.

The described observer is sensitive to motor parameters, especially to the stator resistance. A 20% variation of stator resistance can produce important estimation error.

The Kalman filter based observers use also the mathematical model, but this kind of observers reject measurement noise. The problem with these observers is that tuning the covariance matrices of the model and the measurement errors is rough and requires skilled operators. Another disadvantage of the Kalman filter based algorithms is that they are computationally intensive and time consuming. [Song,2006]

4.2 Initial position detection

Before running the motor, the initial rotor position has to be known at standstill. Having the initial position, two ways of starting the motor arise:

- starting the motor with a simple open loop V\f control to a certain speed, and then close the loop.
- starting directly with Field Oriented Control. In this case the rotor position is considered to be known in order to use it as feedback in the control algorithm.

Several methods have been proposed for the initial angle detection. In [Lukko,2000], a method of estimating the rotor initial position based on measuring the inductance is proposed. The stator inductance of a synchronous machine in the stationary reference frame is defined as in Eq.4.8.

$$L^s{}_s = L_{s0} + L_{s2}cos2\theta_r \tag{4.8}$$

where, L_{s0} and L_{s2} are dependent of L_{sd} and L_{sq}. A new coordinate system of reference is introduced and the stator inductance is redefined as in Eq.4.9

$$L^s{}_s = L_{s0} + L_{s2}cos[2(\theta_r - \lambda)] \tag{4.9}$$

where $\theta_r - \lambda$ is the angle of the rotor in the virtual stationary reference frame. The virtual reference frame is defined as the direction of the stator current used in the inductance measurement. In order to get rid of the measurement error, a model for the inductance is introduced:

$$L^s{}_s = g(t, a) + \epsilon \tag{4.10}$$

A nonlinear leas square method is proposed to fit the measured inductances. The inductance measurement is made in several directions. The current applied to the stator winding will produce torque, which will slightly rotate the rotor during the inductance measurements and affect the method. The rotation is minimized by measuring the next direction always to the opposite direction.

A more detailed explanation of the proposed algorithm and the measurement procedure can be found in [Lukko,2000].

Having the advantage of a sensor mounted on the machine used in this project, the machine is started using FOC and introducing the estimated position and speed afterwards.

4.3 Rotor position and speed estimation

The method chosen for the estimation of the rotor position is based on flux linkage estimation. This method was first proposed by [French,1996]. The algorithm for the flux linkage and rotor position estimation is expressed in α, β stationary reference frame and is divided in 5 steps. A block diagram of the algorithm is presented in Fig.4.4.

As shown in the figure, in the first step, the stator flux linkages are estimated using the measured currents and the voltages. The estimation is made by integrating the difference between the stator voltage and the ohmic voltage drop. Because the integration introduces drift problems in the fourth step the algorithm compensates for the initial prediction errors introduced at this stage. In the second step the currents are estimated, based on the flux linkage estimations from the first step. The current errors are calculated from the measured currents and estimated currents. The error in the predicted rotor position from step five, is corrected in the third step. In the followings, each step of the algorithm is discussed in detail.

Step 1 - Stator flux linkages estimation

In the first step the stator flux linkages are estimated from the stator voltage equations in the stationary reference frame.

$$u_{\alpha,\beta} = R_s i_{\alpha,\beta} + \frac{d}{dt}\Psi_{\alpha,\beta} \tag{4.11}$$

In order to be able to implement the rotor position estimation algorithm in laboratory a discrete model of the estimations is developed. It is assumed that the phase currents and voltages are measured at a fixed sample time T_s, where k is the present sampling interval and $k-1$ is the previous sampling interval. For the discrete integration the rectangular rule is used. The stator flux linkages are:

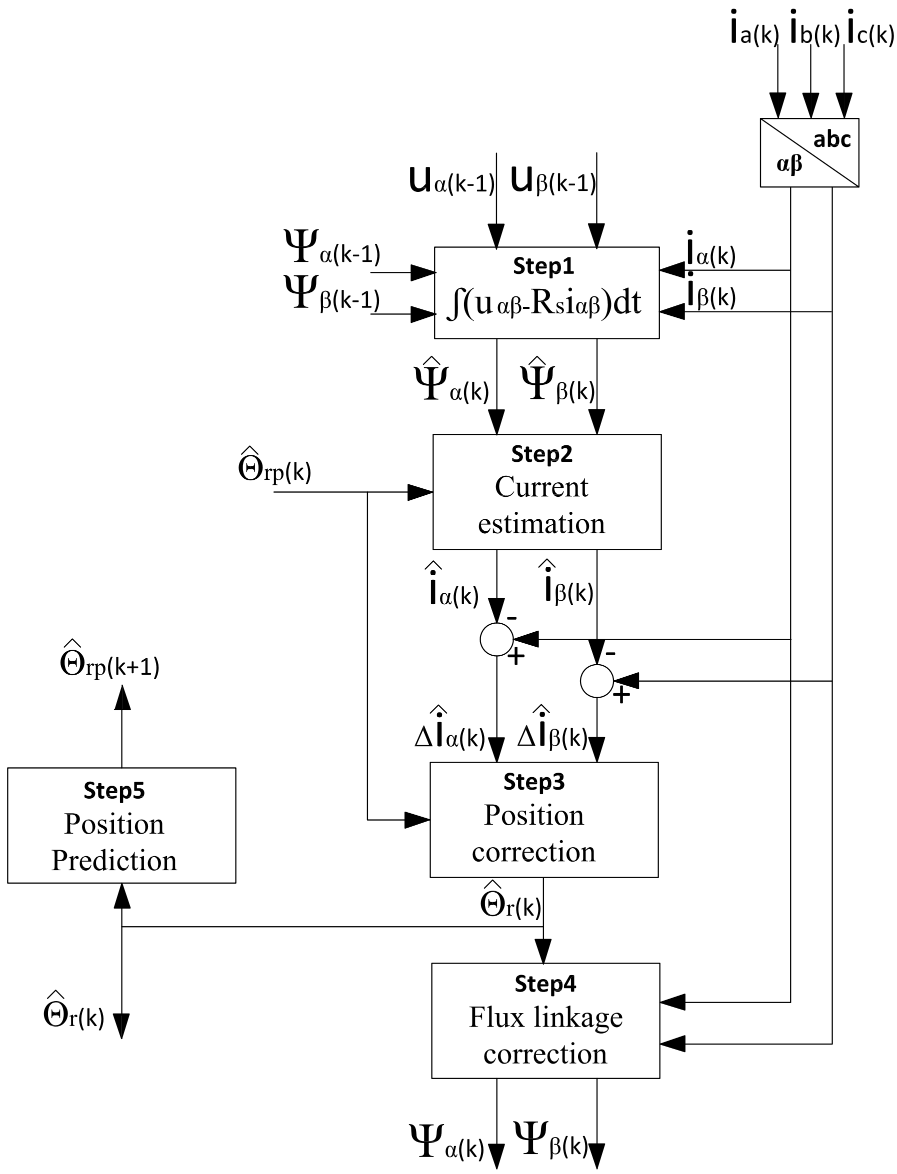

Figure 4.4: *Block diagram of the estimation algorithm for the rotor position*

$$\hat{\Psi}_\alpha(k) = T_s[u^*_\alpha(k-1) - R_s i_\alpha(k)] + \Psi_\alpha(k-1) \tag{4.12}$$

$$\hat{\Psi}_\beta(k) = T_s[u^*_\beta(k-1) - R_s i_\beta(k)] + \Psi_\beta(k-1) \tag{4.13}$$

The input parameters are the $i_\alpha(k), i_\beta(k)$ currents and $u_\alpha(k-1), u_\beta(k-1)$ voltages. The currents are obtained by measuring the a,b,c stator phase currents and by transforming them to the 2 phase stationary reference frame. The voltages are obtained from the controller commanded voltages to the machine in the previous sampling period. As discussed previously, the updated flux values from the previous sampling time are added to the flux values in the present sampling time. The updated flux linkages are obtained in the fifth step. The simulation block of the stator flux linkages estimation is presented in Fig.4.5.

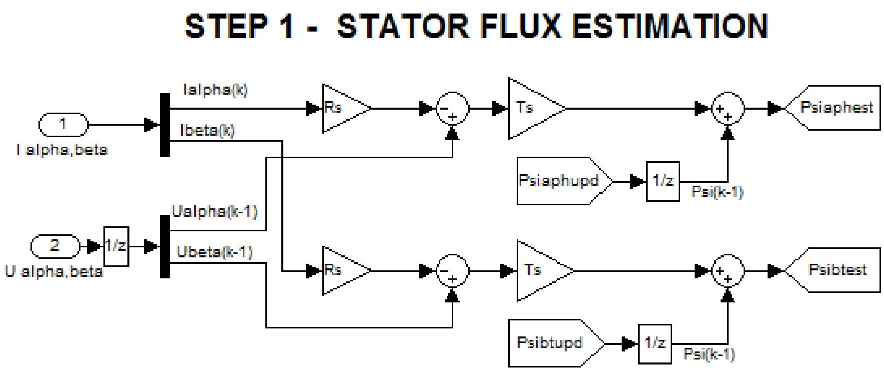

Figure 4.5: *Simulation block of the flux linkages estimation*

Step 2 - Stator current estimation

Based on the flux linkages estimated in step 1 and on the position prediction, the stator currents can be estimated. The stator currents expressions are obtained from the stationary reference frame fluxes Eq.4.14 and Eq.4.15[Chandana,2002]:

$$\Psi_\alpha = -\Delta L sin(2\theta_r) i_\beta + [L - \Delta L cos(2\theta_r)] i_\alpha + \Psi_m cos(\theta_r) \tag{4.14}$$

$$\Psi_\beta = [L + \Delta L cos(2\theta_r)] i_\beta - \Delta L sin(2\theta_r) i_\alpha + \Psi_m sin(\theta_r) \tag{4.15}$$

where,

$$L = \frac{L_q + L_d}{2}$$

$$\Delta L = \frac{L_q - L_d}{2}$$

From Eq.4.14 and the Eq.4.15 the stator currents estimations are determined as in the following equations.

$$\hat{i}_\alpha(k) = \frac{[L + \Delta L cos(2\hat{\theta}_{rp}(k))]\hat{\Psi}_\alpha(k) + \Delta L sin(2\hat{\theta}_{rp}(k))\hat{\Psi}_\beta(k) - (L + \Delta L)\Psi_m cos(\hat{\theta}_{rp}(k))}{L^2 - \Delta L^2} \tag{4.16}$$

$$\hat{i}_\beta(k) = \frac{[L - \Delta L cos(2\hat{\theta}_{rp}(k))]\hat{\Psi}_\beta(k) + \Delta L sin(2\hat{\theta}_{rp}(k))\hat{\Psi}_\alpha(k) - (L + \Delta L)\Psi_m sin(\hat{\theta}_{rp}(k))}{L^2 - \Delta L^2} \tag{4.17}$$

where, θ_{rp} is the predicted position from the fifth step. In Fig.4.6 the simulation block of the stator current estimation is shown.

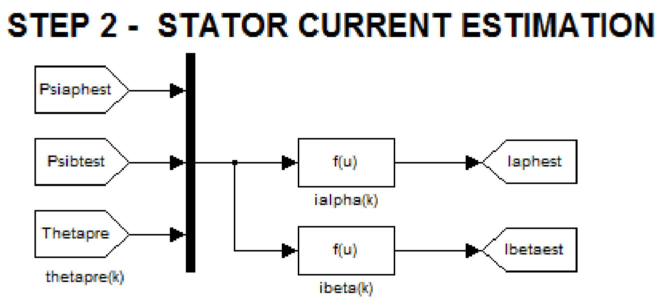

Figure 4.6: *Simulation block of the stator current estimation*

Step 3 - Position correction

In step 5 the rotor position is predicted. In this step the correction of the predicted rotor position is made. For this correction the differences between the measured and the estimated currents from the previous step, i.e. current errors, are used.

$$\Delta i_\alpha(k) = i_\alpha(k) - \hat{i}_\alpha(k) \tag{4.18}$$

$$\Delta i_\beta(k) = i_\beta(k) - \hat{i}_\beta(k) \tag{4.19}$$

In the followings, two methods for the position correction are investigated.

Method 1

The first method is proposed by [French,1996]. Having the current errors, the rotor position can be corrected using the liniarized stationary frame flux equations. [French,1996][Acarnley,1994]. The stationary reference frame fluxes are functions of i_α, i_β and θ_r. The liniarized expressions of the flux equations are presented in Eq.4.20 and Eq.4.21.

$$\Delta\Psi_\alpha = \frac{\partial\Psi_\alpha}{\partial i_\beta}\Delta i_\beta + \frac{\partial\Psi_\alpha}{\partial i_\alpha}\Delta i_\alpha + \frac{\partial\Psi_\alpha}{\partial\theta_r}\Delta\theta_r \tag{4.20}$$

$$\Delta\Psi_\beta = \frac{\partial\Psi_\beta}{\partial i_\beta}\Delta i_\beta + \frac{\partial\Psi_\beta}{\partial i_\alpha}\Delta i_\alpha + \frac{\partial\Psi_\beta}{\partial\theta_r}\Delta\theta_r \tag{4.21}$$

Two assumptions are made:

- the flux estimation from step 1 is accurate $\Rightarrow \Delta\Psi_\alpha = 0$, $\Delta\Psi_\beta = 0$
- the current errors are due to the error in the predicted position

Considering these two assumptions, the position errors are calculated from the current errors.

$$\Delta\theta_\alpha = \frac{-(\frac{\partial\Psi_\alpha}{\partial i_\beta}\Delta i_\beta + \frac{\partial\Psi_\alpha}{\partial i_\alpha}\Delta i_\alpha)}{\frac{\partial\Psi_\alpha}{\partial\theta_r}} \tag{4.22}$$

$$\Delta\theta_\beta = \frac{-(\frac{\partial\Psi_\beta}{\partial i_\beta}\Delta i_\beta + \frac{\partial\Psi_\beta}{\partial i_\alpha}\Delta i_\alpha)}{\frac{\partial\Psi_\beta}{\partial\theta_r}} \tag{4.23}$$

The position error term ($\Delta\theta(k)$) can be obtained by making the average between the position errors calculated previously.

$$\Delta\theta(k) = \frac{\Delta\theta_\alpha(k) + \Delta\theta_\beta(k)}{2} \tag{4.24}$$

Substituting the partial derivatives, the equations for the calculation of $\Delta\theta_\alpha$ and $\Delta\theta_\beta$ are [Chandana,2002]:

$$\Delta\theta_\beta = \frac{-[L + \Delta Lcos(2\hat{\theta}_{rp})]\Delta i_\beta + \Delta Lsin(2\hat{\theta}_{rp})\Delta i_\alpha}{-2\Delta Li_\beta sin(2\hat{\theta}_{rp}) - 2\Delta Li_\alpha cos(2\hat{\theta}_{rp}) + \Psi_m cos(\hat{\theta}_{rp})} \tag{4.25}$$

$$\Delta\theta_\alpha = \frac{\Delta Lsin(2\hat{\theta}_{rp})]\Delta i_\beta - [L - \Delta Lcos(2\hat{\theta}_{rp})]\Delta i_\alpha}{-2\Delta Li_\beta cos(2\hat{\theta}_{rp}) + 2\Delta Li_\alpha sin(2\hat{\theta}_{rp}) - \Psi_m sin(\hat{\theta}_{rp})} \tag{4.26}$$

The problem with these two equations is that the denominators becomes very small at certain levels and a division by zero error occurs.

Method 2

The second method is proposed by [Chandana,2002]. For this method the actual and a predicted rotor reference frame are defined as in Fig.4.7.

The flux in the predicted rotor reference frame is obtained from the flux in the abc reference frame.

$$\underline{\Psi}^p_{qd} = \underline{\Psi}_{abc}e^{-j\hat{\theta}_{rp}} \tag{4.27}$$

The flux expressions obtained are presented in the following equations [Chandana,2002]:

$$\Psi^p_q = Li^p_q + \Delta L[i^p_q cos(2\Delta\theta) - i^p_d sin(2\Delta\theta)] + \Psi_m sin(\Delta\theta) \tag{4.28}$$

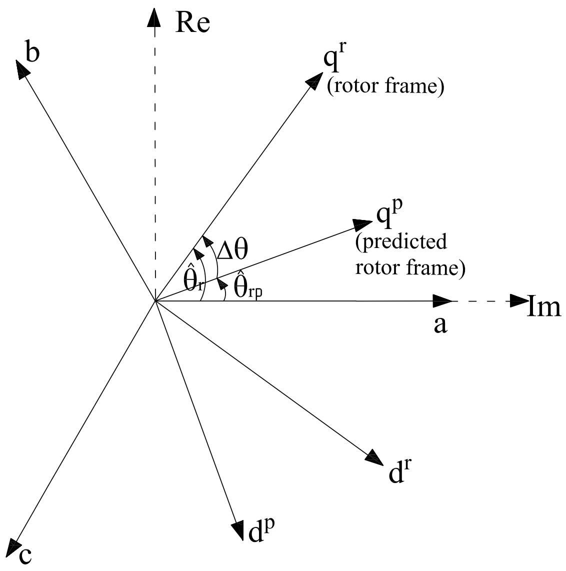

Figure 4.7: *Actual and predicted rotor reference frame [Chandana,2002]*

$$\Psi_d^p = Li_d^p - \Delta L[i_q^p sin(2\Delta\theta) + i_d^p cos(2\Delta\theta)] + \Psi_m cos(\Delta\theta) \tag{4.29}$$

where, $\Delta\theta = \hat{\theta}_r - \hat{\theta}_{rp}$

Assuming that $\Delta\theta$ is very small some approximations are made: $cos(2\Delta\theta) \approx 1$, $cos(\Delta)\theta \approx 1$, $sin(2\Delta\theta) \approx 2\Delta\theta$, $sin(\Delta\theta) \approx \Delta\theta$

Subtracting the actual rotor flux from the predicted rotor flux equations the errors of variables due to the position deviation are obtained.

$$\Delta\Psi_q = L_q \Delta i_q - 2\Delta L i_d^p(\Delta\theta) + Psi_m(\Delta\theta) \tag{4.30}$$

$$\Delta\Psi_d = L_d \Delta i_d - 2\Delta L i_q^p(\Delta\theta) \tag{4.31}$$

For a non-salient pole machine ($\Delta L = 0$), these expressions are simplified as shown in Eq.4.32 and 4.33

$$\Delta\Psi_q = L_q \Delta i_q + Psi_m(\Delta\theta) \tag{4.32}$$

$$\Delta\Psi_d = L_d \Delta i_d \tag{4.33}$$

As it can be seen in the previous equation, the position error appears only in Eq.4.32. Assuming that the flux estimation is accurate in step 1, which means $\Delta\Psi_q = 0$ the position error correction can be obtained as in Eq.4.34.

$$\Delta\theta = \frac{-L_q \Delta i_q}{\Psi_m} \tag{4.34}$$

The current errors Δi_d and Δi_d are obtained by transforming the stationary reference frame current errors into the predicted rotor reference frame as:

$$\Delta i_q = \Delta i_\beta cos(\hat{\theta}_{rp}) - \Delta i_\alpha sin(\hat{\theta}_{rp}) \qquad (4.35)$$

$$\Delta i_d = \Delta i_\beta sin(\hat{\theta}_{rp}) + \Delta i_\alpha cos(\hat{\theta}_{rp}) \qquad (4.36)$$

The corrected position is obtained by adding the position error to the predicted position [Chandana,2002].

$$\hat{\theta}_r(k) = \hat{\theta}_{rp}(k) + \Delta\theta(k) \qquad (4.37)$$

Even though, the machine used in this project presents some saliency, this is neglected, and the Eq.4.34 is used for the position correction.

The simulation block of the position correction is presented in Fig.4.8.

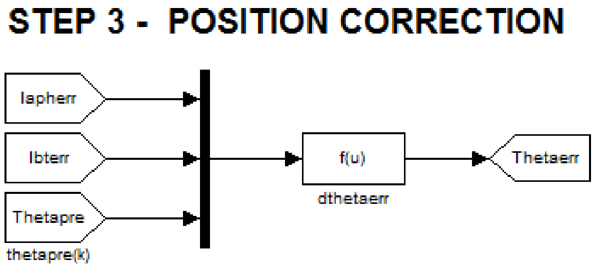

Figure 4.8: *Simulation block of the position correction*

Step 4 - Flux linkages updating

In this step, the fluxes are recalculated using the corrected rotor position and the measured stator currents. The equations 4.14 and 4.15 are transformed in discrete time.

$$\Psi_\alpha(k) = [L - \Delta Lcos(2\hat{\theta}_r(k))]i_\alpha(k) - \Delta Lsin(2\hat{\theta}_r(k))i_\beta(k) + \Psi_m cos(\hat{\theta}_r(k)) \qquad (4.38)$$

$$\Psi_\beta(k) = [L + \Delta Lcos(2\hat{\theta}_r(k))]i_\beta(k) - \Delta Lsin(2\hat{\theta}_r(k))i_\alpha(k) + \Psi_m sin(\hat{\theta}_r(k)) \qquad (4.39)$$

The updated fluxes are used in the next sampling time to estimate the fluxes in the first step of the algorithm. In this way, the drift introduced by the integration in step 1 can be avoided.

The block diagram of the flux linkages updating is presented in Fig.4.9.

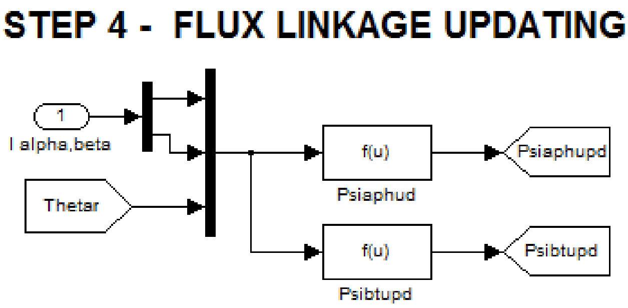

Figure 4.9: *Simulation block of the position correction*

Step 5 - Rotor position prediction

Considering that position varies with time as a second-order polynomial, the position prediction can be expressed as a polynomial function as shown in Eq.4.40.[French,1996]

$$\theta_{rp} = At^2 + Bt + C \tag{4.40}$$

where, A,B,C are the coefficients of the quadratic function.

In Fig.4.10 the principle of rotor position prediction using the polynomial curve fitting is presented. By using three estimated previous positions, at (k-2), (k-1), (k) sampling instants the A, B, C coefficients can be determined.

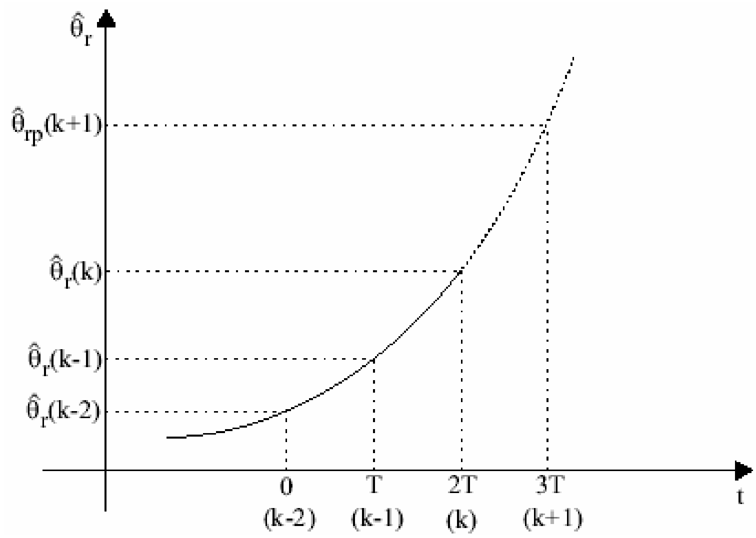

Figure 4.10: *Rotor position prediction using polynomial curve fitting [Chandana,2002]*

Assuming t=0 at (k-2) sampling time, the rotor position can be expressed as:

$$\hat{\theta}_r(k-2) = C \tag{4.41}$$

t=1 at (k-1) sampling instant:

$$\hat{\theta}_r(k-1) = AT_s^2 + BT_s + C \tag{4.42}$$

t=2 at (k) sampling instant:

$$\hat{\theta}_r(k) = A(2T_s)^2 + B(2T_s) + C \tag{4.43}$$

At (k+1) sampling instant the predicted position is:

$$\hat{\theta}_{rp}(k+1) = A(3T_s)^2 + B(3T_s) + C \tag{4.44}$$

From Eq.4.41, Eq.4.42 and Eq.4.43, A,B,C are obtained and by substituting them in Eq.4.44, the rotor position can be predicted at (k+1) sampling instant.

$$\hat{\theta}_{rp}(k+1) = 3\hat{\theta}_r(k) - 3\hat{\theta}_r(k-1) + \hat{\theta}_r(k-2) \tag{4.45}$$

In Fig.4.11 the simulation block of the rotor position prediction is presented.

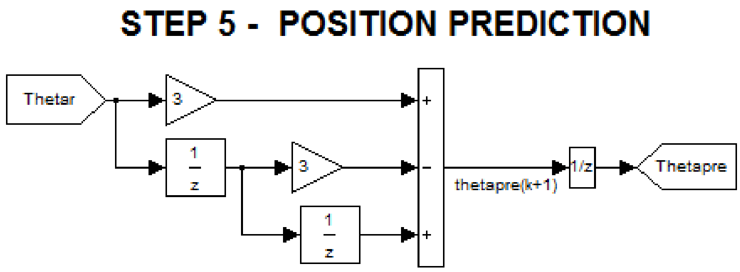

Figure 4.11: *Simulation block of the position correction*

In the presented algorithm the saliency of the machine was neglected, which means that $\Delta L = 0$.

4.4 Simulation results

In this section, the simulation results of the implemented algorithm for the position and speed estimation are presented. The estimators are first tested in open loop and afterwards in closed loop.

Open loop

The open loop test is performed by running the machine, at the nominal speed ($n = 1750[rpm]$). First the machine is run at no load. After 0.5[sec] the machine is run in motor mode at half rated torque ($T_L = 6[Nm]$) and after 1[sec] in generator mode at rated torque ($T_L = 12[Nm]$). In figure 4.12 (a) and (b) the measured and estimated values of the d and q axis fluxes, are presented. As shown in the figure, the estimated fluxes follow with

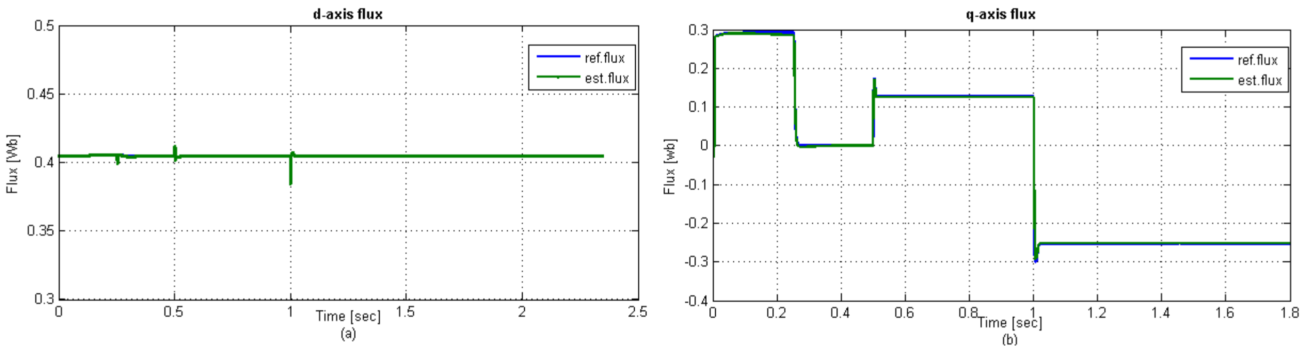

Figure 4.12: *Measured and estimated fluxes: (a) d-axis flux (b) q-axis flux*

good accuracy the measured fluxes.

The measured and estimated rotor position are shown in Fig.4.13 (a). In Fig.4.13 (b), the measured and estimated speed are presented. As shown in the figure, when the load

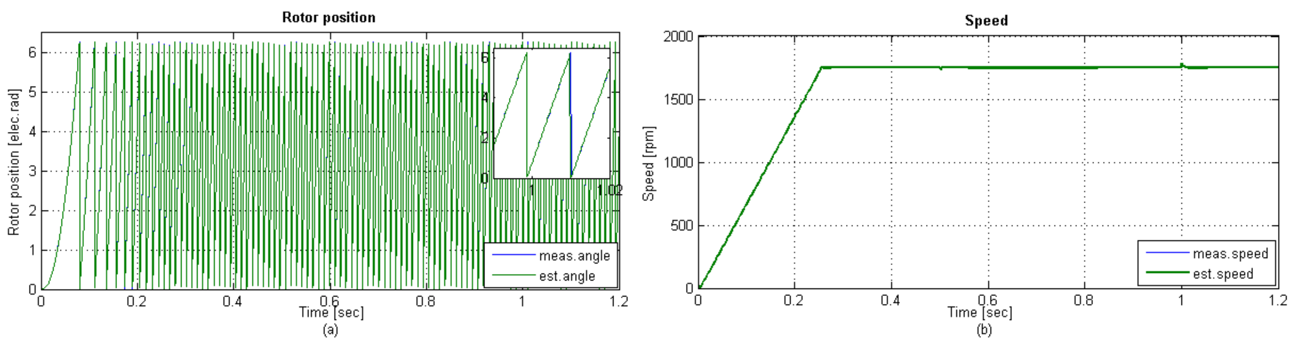

Figure 4.13: *Measured and estimated: (a) Rotor position (b) Speed*

torque is applied at 1[sec] there is a small error in the rotor position estimation.

Closed loop

The machine is tested in closed loop at different conditions in order to see the behavior of the position and speed estimations.

The estimators are introduced at 0.07[sec], at approximately 500[rpm]. For the estimated speed a low pass filter of 40Hz is used.

The machine is run at nominal speed with no load. A load step of 50% rated torque is applied at 1[sec] and another load step to rated torque is applied at 2[sec].

The values of the measured and estimated fluxes are presented in Fig.4.14.

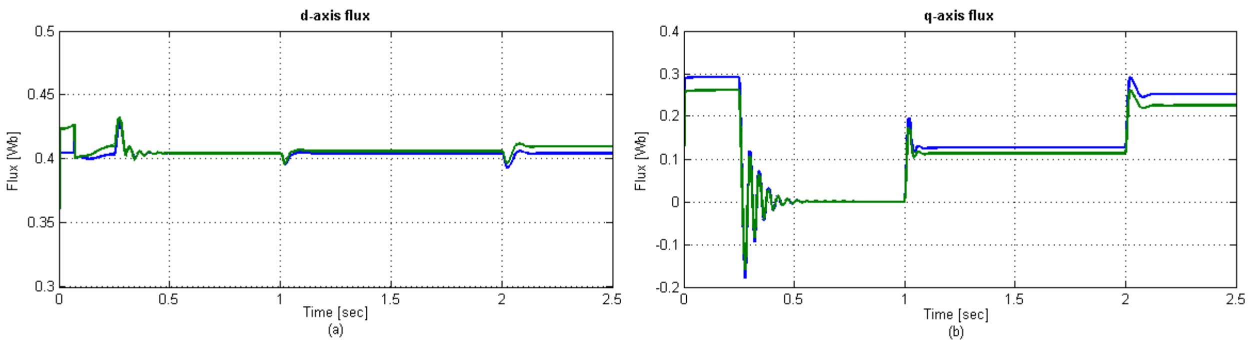

Figure 4.14: *Measured and estimated fluxes: (a) d-axis flux (b) q-axis flux*

As it can be observed in Fig.4.14, at no load there is no error between the measured and the estimated flux. The error increases with the load. It can be seen that the highest error is at the rated load torque.

In Fig.4.15 the estimation of the position is shown. As presented for the fluxes, at no load there is no error. The error increases with the load. In the zooms made in the figure it can be seen the position error at no load, at 50% load and at rated load torque. The

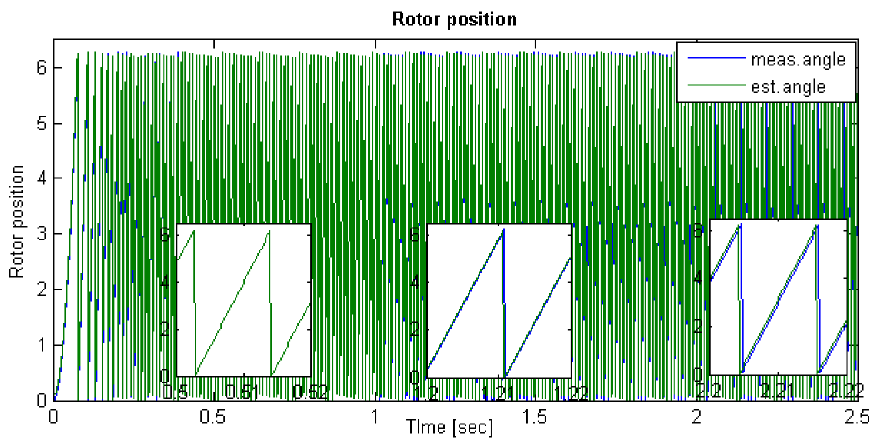

Figure 4.15: *Position estimation for different load torque*

electromagnetic torque and the measured speed, with the position and speed estimations, are shown in Fig.4.16 (a) respectively (b).

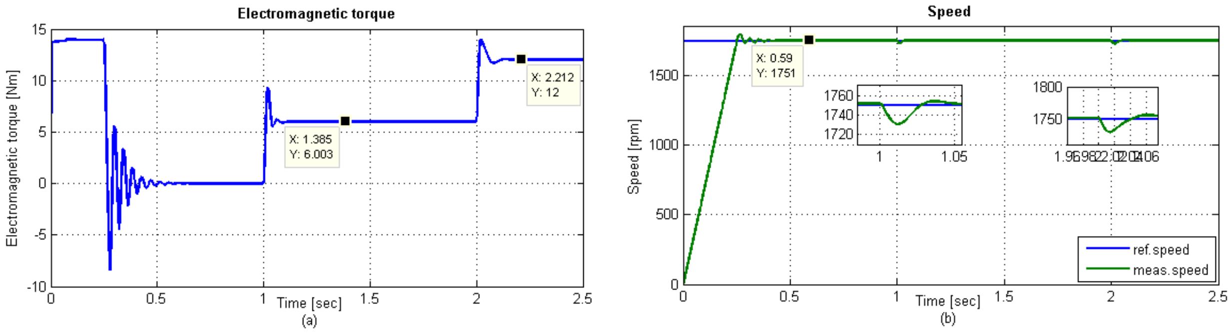

Figure 4.16: *Motor operation at different load torques, with the position and speed estimations: (a) Electromagnetic torque (b) Reference and measured speed*

It can be seen in Fig.4.16 (b), that the speed response has a settling time of approximately 0.5[sec] and an overshoot of 2.6% which are higher when using the position and speed estimations than with the measured values. This causes also oscilations in the torque, as shown in Fig.4.16 (a). The speed follows the reference, with a small error of 1[rpm].

A reason why the error in position estimation increases with the load may be the fact that the saliency of the machine was neglected in the algorithm for position estimation. Also in the third step, some approximations are taken and only a single position correction term is used (Eq.4.34).

Another test is made to check the behavior of the position and speed estimation in generator operation of the machine.

The machine is started at no load with a rated speed step and it is run in motor mode at nominal load torque after 1[sec] and in generator mode after 2[sec].

The position and speed estimations are as shown in Fig.4.17.

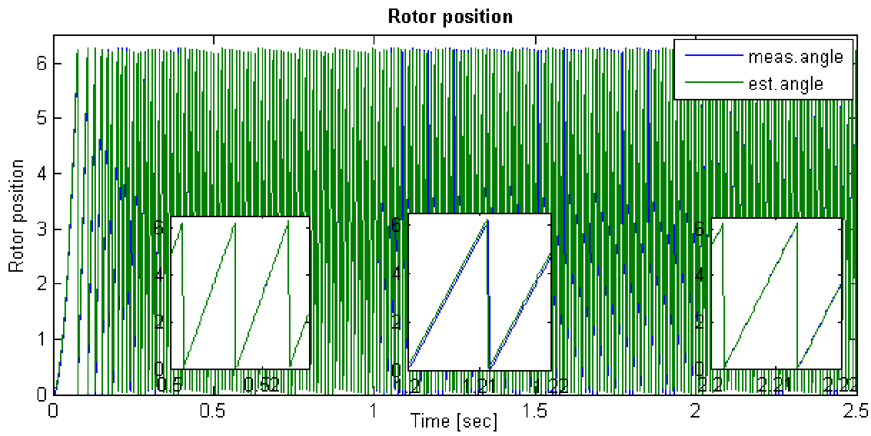

Figure 4.17: *Position estimation at nominal load torque for motor and generator operation*

The same behavior presented in the previous test is observed for the motor operation with load. For the generator operation at the nominal load torque, it can be observed that the error between the estimated and reference value is reduced.

In Fig.4.18(a) and (b) the electromagnetic torque, respectively the reference and the measured speed are shown.

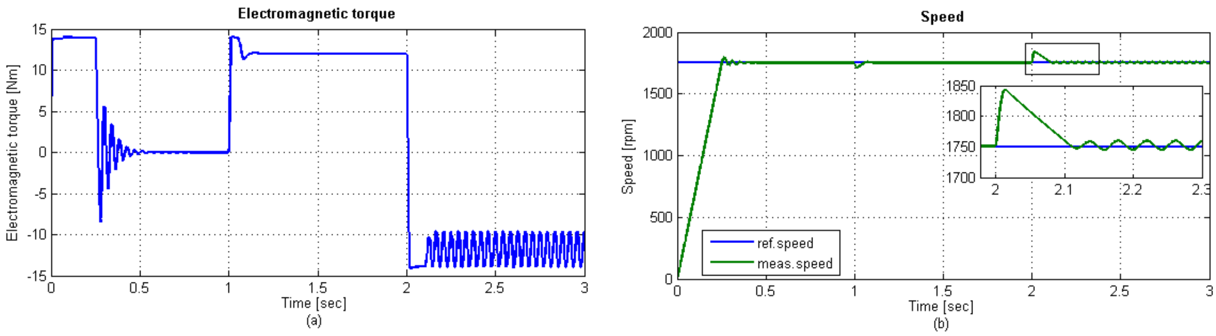

Figure 4.18: *Motor and generator operation at nominal load torque: (a) Electromagnetic torque (b) Reference and measured speed*

From Fig.4.18 (a) and (b), it can be seen that during the generator operation oscillations appear. Taking in consideration that the position estimation is following the reference, it can be stated that the oscilations are introduced by the speed estimation.

Conclusions

In this chapter, several methods for the position and speed estimations were presented. One method was chosen and simulated. The results were presented for different conditions. The method shows good behavior of the estimators at no load. It was noticed that there is an error between the measured and the estimated position in the motor operation, which increases with the increase in load. It was observed that during the generator operation oscilations appeared.

5

Laboratory implementation

The purpose of this chapter is to present the laboratory work. The chapter begins with a description of the system configuration, where the main components of the test setup are presented. The real time interface is presented in the next section. In the last part of the chapter, the laboratory results are presented and discussed.

5.1 Test setup

In this section the configuration of the test setup is presented. The block diagram of the setup is presented in Fig.5.1. In the figure, the main blocks and the signals between them are presented.

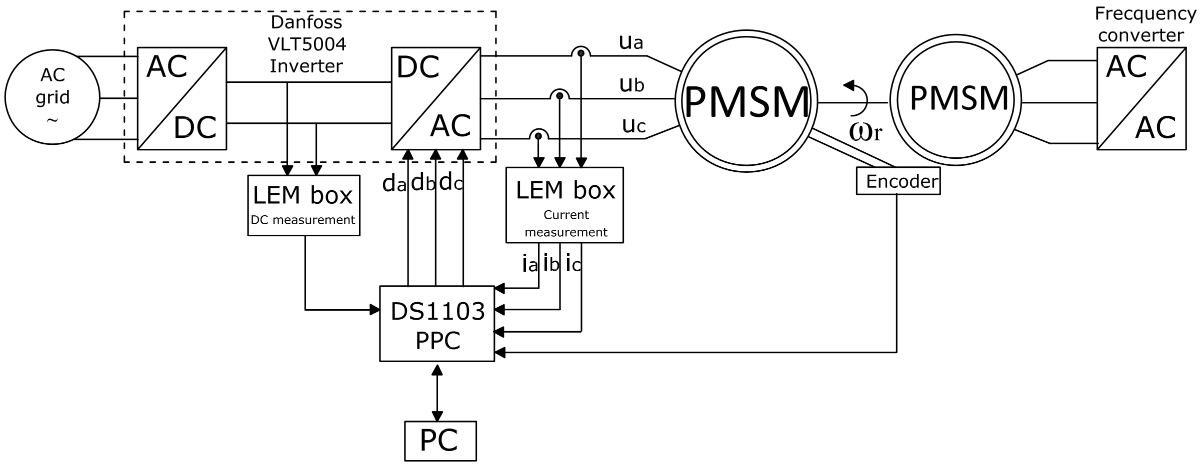

Figure 5.1: *Block diagram of the test setup*

The main components of the system are:

- PM Synchronous Machine
- Danfoss VLT 5004 inverter
- Siemens PMSM type ROTEC 1FT6084-8SH7
- Siemens SIMOVERT MC DC inverter type 6SE7022-6TC51-ZC23

- 2 LEM boxes A LEM box is a card which contains transducers mounted in a plastic box. [Teodorescu,2003] In this setup two LEM boxed are used:

  - one LEM box used for the U_{DC} measurements (1 voltage transducer)

  - one LEM box used for the stator currents i_a, i_b, i_c measurements (3 current transducers)

- DS1103 PPC digital controller - which is built as a PC card that can be mounted into a slot of the motherboard of the host PC

The specifications of the system components are presented in Appendix B

The PM synchronous machine is described in section 2.4, Chapter 2. The machine is connected to another PMSM. The setup is presented in Fig.5.2.

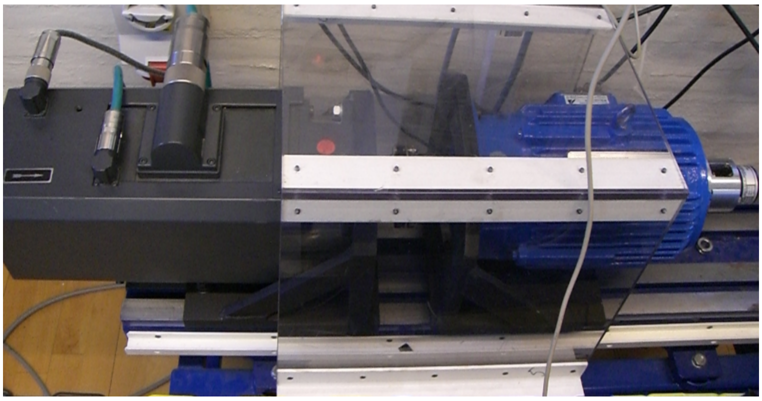

Figure 5.2: *Setup of the machines*

As it can be seen in Fig.5.1, the machine is supplied with a 3 phase voltage from the Danfoss VLT inverter. The VLT5004 frequency inverter is a standard IGBT-VS inverter where the original control card has been replaced by a special Interface and Protection Card (IPC), that enables the IGBT drivers to be controlled from an external digital controller providing reliable short-circuit, shoot-through, dc-overvoltage and over temperature protections.[Teodorescu,2003]

The inverter is controlled by the DS1103 PPC digital controller. The DS1103 is a single board system based on the Motorola PowerPC 604e/333MHz processor (PPC), which forms the main processing unit. It has a software SIMULINK interface that allows all applications to be developed in Matlab/Simulink. All compiling and downloading processes are carried out automatically in the background. A software called Control Desk, allows real-time management of the running process by providing a virtual control panel with instruments and scopes.[Teodorescu,2003]

For control of the machine the measurements of the DC voltage and currents are needed. These measurements are done using the two LEM boxes.

In the next section the real time interface is presented.

5.2 Real time interface

The designed control needs to be tested in real time application in order to check its performances. Therefore, it is decided to implement the control in dSpace platform, mounted in one of the laboratory of Aalborg University.

One advantage of using dSpace is that, is able to provide online computation and updating, which fulfill the main demand of the tests. Another advantage is that dSpace automatically generates the real time code and data for online monitoring. As mentioned before, the cooperation with Matlab/Simulink is another major advantage.

The real time interface has been designed as a Simulink blockset. It consists mainly of two principal blocks: the **MEASURE&CONTROL block**, which is connected to the **FOC&Position estimation** where the algorithm is implemented. These two blocks are as shown in Fig.5.3.

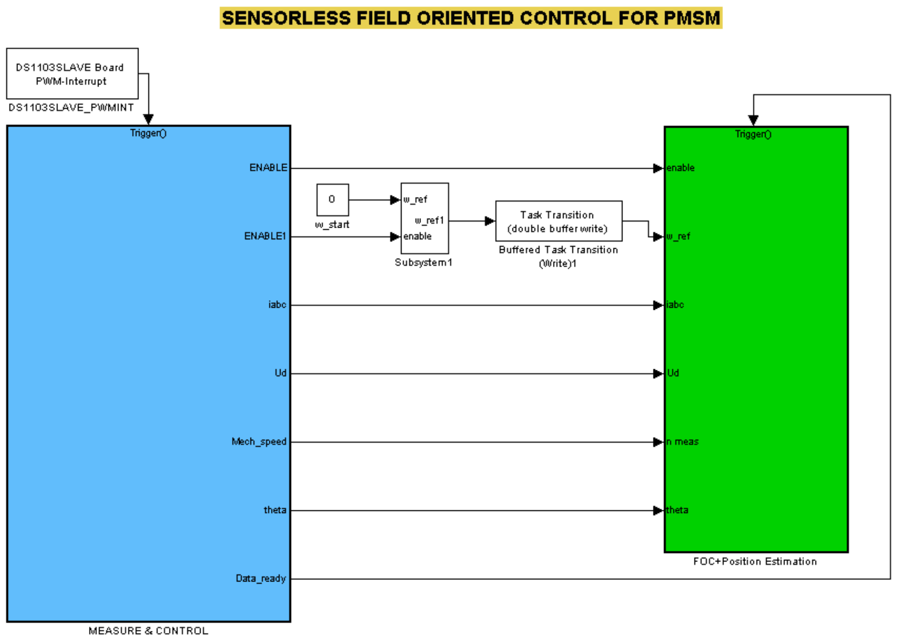

Figure 5.3: *Main blocks of the Real Time Interface*

The MEASURE&CONTROL block consists of a couple of modules. Each of them is used to ensure, that the loaded program and the entire application run properly. The main parts of the MEASURE&CONTROL block are:

- Control block
- Current measurement block
- DC link voltage measurement block
- Speed measurement block
- Protection block

In the **Control block**, the command for enabling or disabling the inverter is found. The algorithm is build such that if any fault occurs, the converter is stopped. The currents measurement interface is found in the **Current Measurement block**. The value of the DC voltage is given by the **DC Link Voltage Measurement block**. The DC voltage is used to create the three phase voltages, used to supply the machine. As there is no feedback from the voltage sensors, the DC voltage is employed as the basis for the algorithm. Having also an encoder mounted on the shaft, the position and rotational speed are read from the **Speed Measurement block**. These information are necessary for the control of the PM synchronous machine. The **Protection block** consists of a couple of protections, preventing the system from failing. There are overvoltage, overspeed, shortcircuit and undervoltage protections. If any of these failures occur, it results in generating signal passed to **Control block**, which stops entire system. The RTI Simulink blockset is provided by the Aalborg University and modified for the sake of the project.

In the FOC&Sensorless block, the FOC using a sensor and the estimation of the position algorithm are implemented. In the next section the experiments performed and the results are presented.

5.3 Results

In this section, the experiments that were made in order to check the designed control, are presented. Also the results are presented and discussed. The software used for the results presentation is Control Desk. This software provides the necessary functions for control and also for real time-monitoring the results. In order to see the results, a graphical interface has been created. The Control Desk layout is presented in Fig.5.4.

In order to run the PMSM as a generator, the test setup needs to be modified in order to be able to dissipate the produced power. Due to the time limitation, the FOC control strategy is implemented to control the permanent magnet synchronous machine only in motor mode.

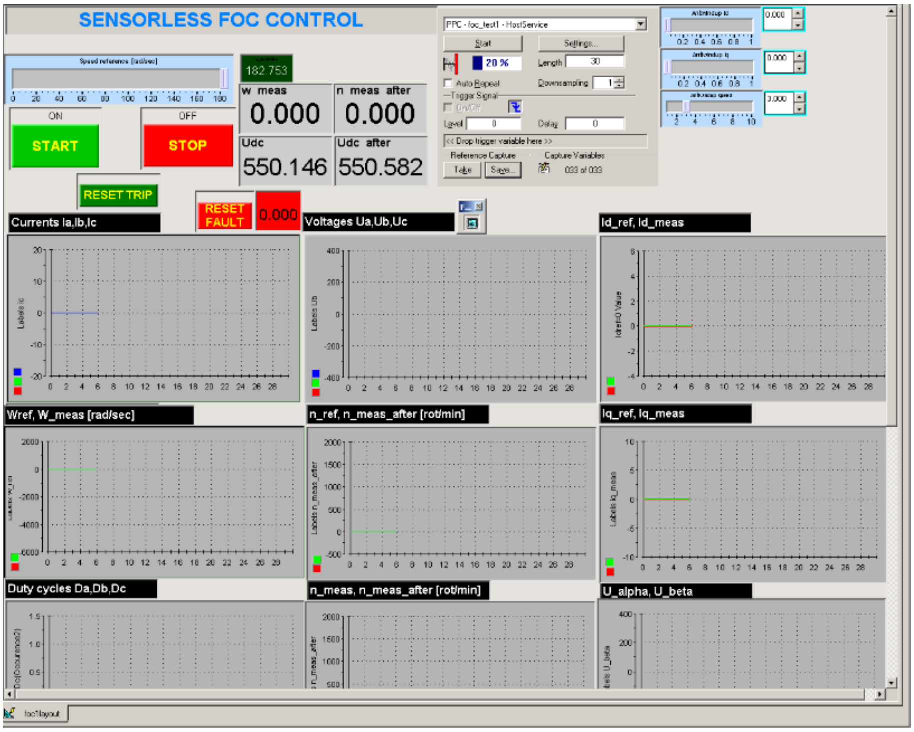

Figure 5.4: *Simulation block of the position correction*

5.3.1 Field Oriented Control with speed encoder

In this section the FOC with SVM, using the speed encoder attached on the PMSM, is tested and its performances are presented for different cases.

Motor operation at no load, steps in speed

For this test the machine was started with a reference speed step of 50% the rated speed ($n = 875[rpm]$) at no load. Another step to the rated speed($n = 1750[rpm]$) was applied at 6.9[sec] and a negative step to 800[rpm] was applied at approximately 20[sec].

The measured voltages and currents are represented in Fig.5.5 (a) respectively (b).

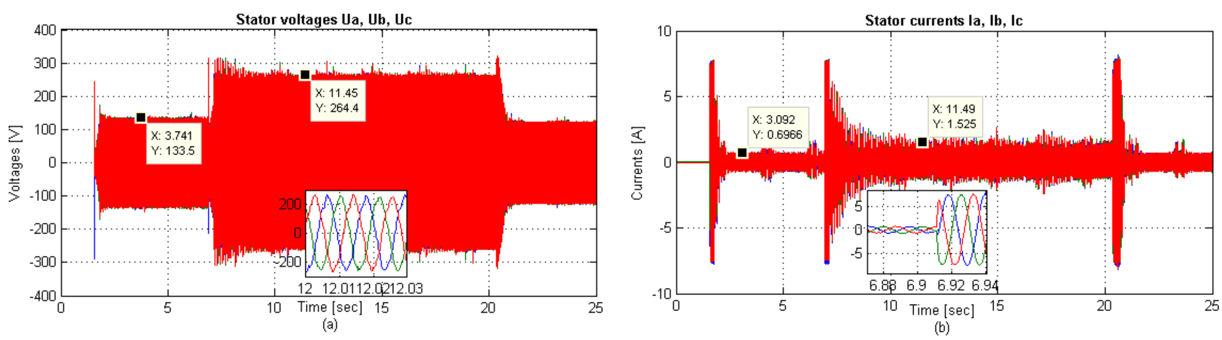

Figure 5.5: *Measured voltages and currents at different speed steps: (a) Stator voltages (b) Stator currents*

As shown in Fig5.5 (a), the voltages amplitude at 50% rated speed, is 133,5[V] which close to the value obtained from the simulation at the same conditions 111[V]. At the rated speed the amplitude of the voltages is 264.4[V] which is comparable to the one in the simulations 222.1[V], (see Chapter 3, section3.4.1). The difference between the simulated and the measured values of the voltages may be due to the fact that the parameters of the machine used in the simulation are different from the real ones. In Fig.5.5 (b), when the steps are applied, during the acceleration of the machine to the reference speed, the currents are limited to the same value as used in the simulations 7.6[A]. It can also be seen that at 50% rated speed the value of the currents is 0.69[A]. Also the amplitude is increasing to 1.52[A] when the speed is increased to rated speed. This values are normal due to the fact that in real implementation, unlike in the simulations, there is some torque produced to overcome the dry friction torque and the viscous friction of the machine.

In Fig.5.6, the speed response to the applied steps is shown.

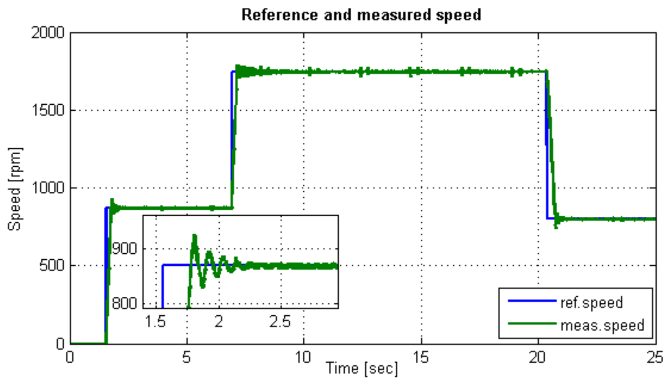

Figure 5.6: *Reference and measured speed at different speed steps*

The machine is started with a step of 875[rpm]. It can be seen in Fig.5.6 that the measured speed is following the reference. In the zoom made, it is shown that the response presents an overshoot of 5.7% and the settling time is approximately 0.75[sec].

Motor operation at 50% rated speed, 50% rated torque, step in speed to nominal speed

The machine is started at 50% rated speed ($n = 875[rpm]$). A step of 2[Nm] is applied after 4[sec] and afterwards the torque is gradually increased to 50% rated torque ($T_L = 6[Nm]$). A step in speed to nominal speed is applied at approximately 12[sec].

The measured voltages and currents for the presented conditions are as shown in Fig.5.7 (a) respectively (b).

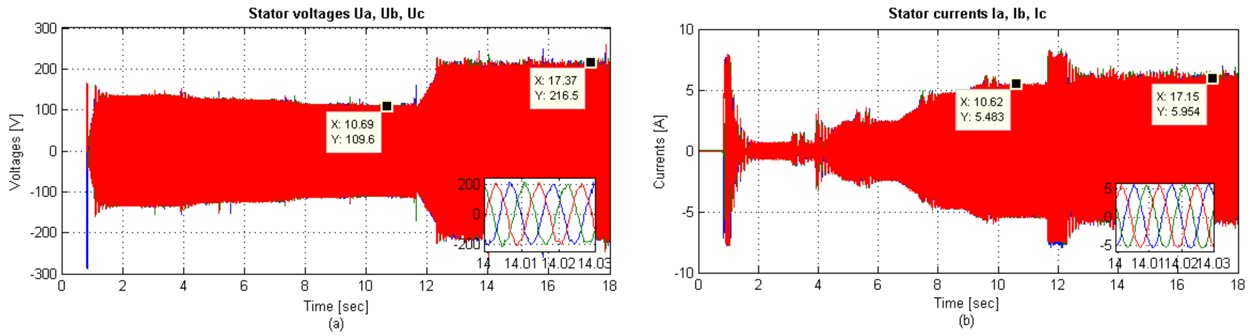

Figure 5.7: *Measured voltages and currents at different conditions: (a) Stator voltages (b) Stator currents*

As it can be seen in Fig.5.7 (a), the voltages are decreasing when the load torque is applied. This behavior is due to the fact that during this time the DC link voltage was also decreasing. At 50% rated speed and 50% rated torque, the voltage amplitude is approximately 110[V]. This is comparable to the value obtained from the simulations 122.5[V](see Chapter 3, section 3.4.2). In Fig.5.7 (b) the currents are shown. In can be seen that the currents are increasing with the load. The amplitude of the currents at 50% rated speed and 50% rated torque, is approximately 5.5[A]. This value is bigger than the one obtained in the simulations 3.3[A]. One reason for this difference it can be that the load is not properly controlled and the applied torque is different than the measured one. Another test to sustain this idea is shown in a laboratory jurnal presented in AppendixC. Another reason could be that the machine parameters in the real system are different than the ones used in the simulation.

The Id and Iq currents are presented in Fig5.8 (a) and (b). As shown in Fig.5.8 (a),

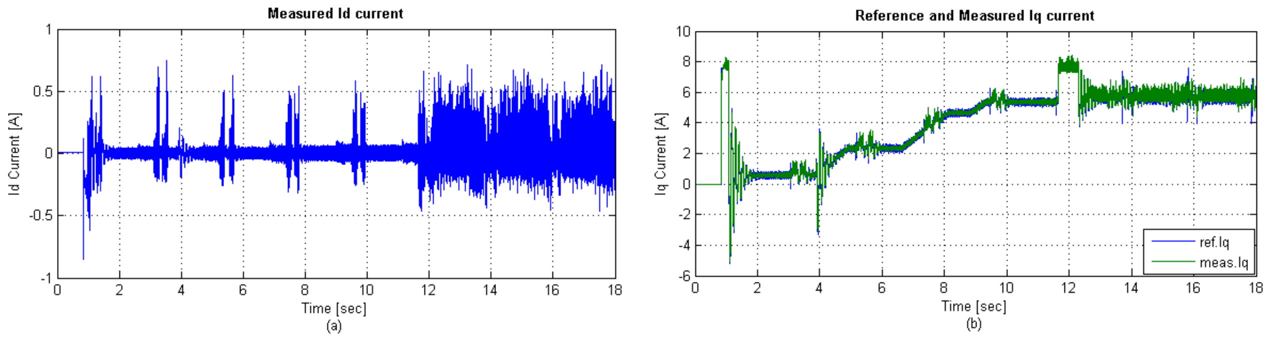

Figure 5.8: *Currents: (a) Measured Id (b) Reference and measured Iq*

the I_d current is approximately zero. From Fig.5.8 (b), it can be seen that the measured I_q current is following the reference values.

The speed response to the applied steps in speed and torque is presented in Fig.5.9. It can be observed, in Fig.5.9, that the measured speed is following the reference one. A zoom is made in the picture to show the step response and the moment when the torque is applied at 4 [sec]. Also in the measurements, like in the simulations, the speed response is slower when the step in speed is applied to the loaded machine.

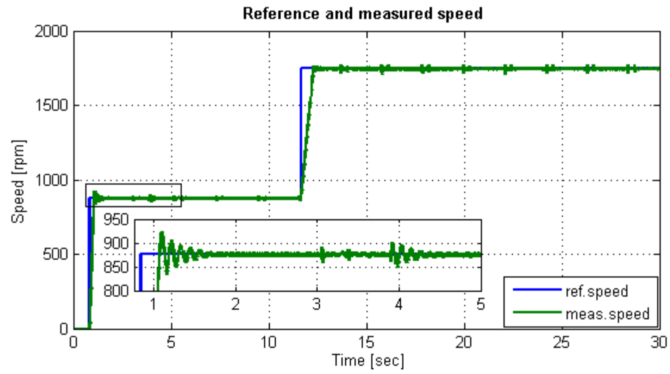

Figure 5.9: *Reference and measured speed*

5.3.2 Position and speed estimation

The position and speed estimations were tested in open loop. The machine was runned at no load and no signal from the estimators could be detected. This is due to the fact that a signal in the estimation algorithm is not a number. Having an algorithm where all the signals are dependent of each other, one not-a-number signal will lead to all of them being the same. Considering that the algorithm is working in the simulations but not in dSpace, it is considered to be a numerical stability problem.

In order to check the flux linkages estimations, the measured position was used as input to step 4 and 5 from the estimation algorithm. The reference and the estimated d and q-axis fluxes are presented in Fig.5.10.

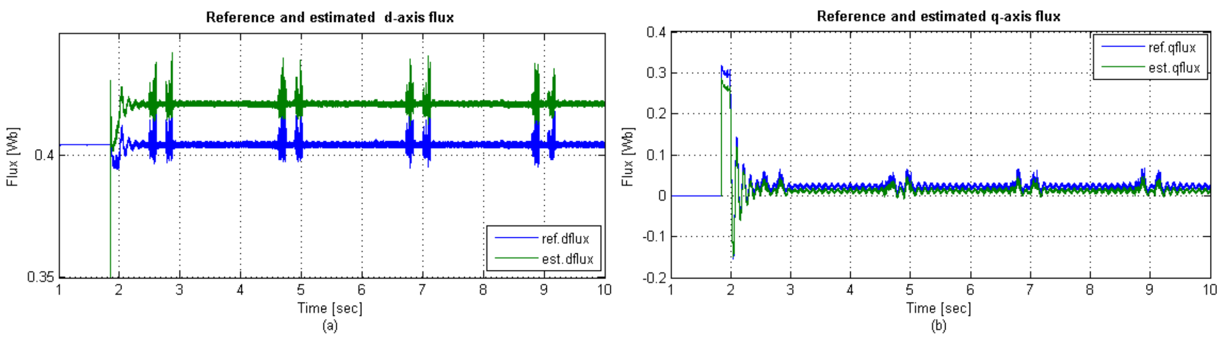

Figure 5.10: *Reference and estimated flux: (a) d-axis flux (b) q-axis flux*

It can be seen in the figure, that the estimations are following the references, even if an error occurs.

Conclusions

In this chapter the laboratory work was presented. The test setup and the real time interface were introduced. The FOC with sensor was tested and the results show that the control is working. Testing the machine with the load, a difference between the measured and the simulated currents was found. This error was attributed to the fact, that the load is not *properly controlled or there is an error bethween the parameters used in the simulation and the real ones. The estimated position and speed were tested next in open loop, but no signal could be detected. This is caused by numerical problems in the proposed algorithm.*

6 Conclusions

The main objective of this project is to develop a sensorless control on a surface mounted PMSM for wind turbine applications. In order to fulfill this objective, several goals were stated in Chapter 1:

- design a sensored control structure for a surface mounted PMSG;
- investigate methods used for the sensorless control;
- choose a method and investigate its performances on a 2.2[KW] generator in Matlab/Simulink;
- laboratory implementation of the sensored control in dSpace;
- laboratory implementation of the sensorless control in dSpace;
- if the sensorless method shows satisfactory results, simulation of the sensorless control on a 2-3[MW] generator.

A sensored Field Oriented Control structure was first designed. The control was simulated in Matlab/Simulink and tested for different conditions. The results presented showed good performances of the control.

Further, methods for the position and speed estimation were investigated. A method based on flux linkage estimation was chosen and simulated. The method uses the measured currents and the voltages. In the simulations, the position and speed estimations were tested in open and closed loop. The results showed good behaviour of the estimations, the reference position following the measured one. It was observed that an error, between the reference and the measured angle, occurred when the load torque was applied.

The presented method is a simple method and does not require any signal injection, which makes it suitable for wind turbine applications. From the load point of view, in a wind turbine system, the load has slower dynamics. Due to the decreased dynamics of torque applied to the generator, the requirements on the sensorless control method are reduced.

The FOC with the measured speed from the encoder mounted on the rotor, was tested in laboratory, in dSpace. The results showed good response of the control with no load.

When applying the load, it was observed that the amplitude of the currents was higher than expected. The speed response to different steps showed good behavior in all the presented conditions.

The position estimation method, was also tested in the real system, in dSpace. No signal could be detected. This was due numerical stability issues given by the implemented algorithm.

As a conclusion, a sensored Field Oriented Control was implemented on a 2.2[kW] PMSM. Testing the control in laboratory good performance was obtained. The method investigated for the position estimation proved to be working in the simulation, but could not be implemented in dSpace.

Future work

Not being able to reach all the goals, there are several tasks to be made as future work:

- tests should be made in laboratory with the PMSM running as generator;
- the method for the rotor position and speed estimation should be investigated more in the laboratory, in order to solve the numerical stability issues;
- with the method working properly, the sensorless control should be investigated on a 2-3[MW] generator.

Bibliography

[Acarnley,1994] N. Ertugrul, P.P. Acarnley, *A New Algorithm for Sensorless Operation of Permanent Magnet Motors*, IEEE Transactions on Industry Applications, Vol.30, No.1, January-February 1994

[AC Machines,2008] *Advanced control of AC Machines* - Lecture slides, PED 8, Spring 2008, Aalborg University

[Brahmi,2008] J. Brahmi et al., *A comparative study between three sensorless control strategies for PMSG in wind energy conversion system*, Appl Energy, 2008

[Chandana,2002] P.D.Chandana Perera, *Sensorless Control of Permanent-Magnet Synchronous Motor Drives*, Ph.D Thesis, AAU-IET, 2002

[Fatu,2008] Marius Fatu, *High Performance Control of PMSG for Wind Energy Conversion*, Ph.D. Thesis, Timisoara, 2008

[Franklin,2006] Gene F. Franklin, J.D. Powell, A. Emami-Naeini, *Feedback Control of Dynamic Systems*, Fifth Edition, Prentice Hall, USA, 2006, ISBN 0-13-149930-0

[French,1996] Chris French, Paul Acarnley, *Control of Permanent Magnet Motor Drives Using a New Position Estimation Technique*, IEEE Transactions on Industry Applications, vol.32, no. 5, 1996

[Grauers,1996] Anders Grauers, *Design of Direct-driven Permanent-magnet Generators for Wind Turbines*, Technical Report No. 292, Department of Electric Power Engineering, Goteborg, 1996

[Kazmierkowski,2002] , M.P. Kawmierkowski, R. Krishnan *Control in Power Electronics. Selected problems*, Academic Press, USA, 2002, ISBN 0-12-402772-5

[Kazmierkowski,1995] M.P. Kawmierkowski, H. Tunia, *Automatic Control of Converter-Fed Drives*, Elsevier, ISBN 0-7803-1101-9, 1995

[Li,2008] S. Li, Tim A. Haskew, *Characteristic Study of Vector-Controlled Direct Driven Permanent Magnet Synchronous Generator in Wind Power Generation*, IEEE, 2008

[Lukko,2000] Julius Lukko, *Direct torque control of permanent magnet synchronous machines - analysis and implementation*, Lappeenranta, 2000, ISBN 951-764-438-8

[Mizera,2005] R. Mizera, *Modification of Symmetric Optimum Method*

[Patel,2006] Mukund R. Patel, *Wind and Solar Power Systems. Design, Analysis, and Operation*, Second Edition, Taylor & Francis Group, New York, 2006, ISBN-13: 978-0-8493-1570-1

[Quaschning,2006] Volker Quaschning, *Undestanding Renewable Energy Systems*, Earthscan, London, 2006, ISBN: 1-84407-128-6

[Teodorescu,2003] R. Teodorescu, *Getting started with dSPACE system*, Aalborg University, Institute of Energy Technology, Department of Electrical Energy Conversion, Version 2003

[Senjyu,2007] Tomonobu Senjyu, Endusa B. Muhando et all, *Maximum Wind Power Capture by Sensorless Rotor Position and Wind Velocity Estimation from Flux Linkage and Sliding Observer*, International Journal of Emerging Electric Power Systems, vol.8, 2007

[Song,2006] Z. Song et al., *Sensorless control of surface permanent magnet synchronous motor using a new method*, Energy Conversion and Management, 2006

[Timbus,2003] Adrian V. Timbus, *Sensorless Control of Permanent Magnet Synchronous Motor*, Master Thesis, Aalborg University, 2003

[Vas,1998] Peter Vas, *Electrical Machines and Drives*, Oxford University Press, 1992

[Yin,2007] Ming Yin et all, *Modeling of the Wind Turbine with a Permanent Magnet Synchronous Generator for Integration*, 2007

Summary

The objective of the present project is to design a sensorless field oriented control (FOC) on a surface mounted PMSG for wind turbine applications. The project was a proposal from Siemens Wind Power. In order to be able to implement the control in laboratory the control was designed for a 2.2[kW] PM machine. First a sensored control is simulated and implemented in laboratory, in Dspace. A method for position and speed estimation is also investigated. In the followings a short description of each chapter is presented.

In the first chapter an introduction to the project is presented. The problem formulation, the objectives and the project limitations are stated. At the end of the chapter, the report structure is presented.

In the second chapter the system is described. The converter and the control strategy for the duty cycle generation, space vector modulation (SVM) are presented. A short presentation of the permanent magnet synchronous machine is also made. In order to be able to simulate the machine, the mathematical model is developed. The results of the simulation are presented at the end of the chapter.

The third chapter presents the control strategy. An introduction to Field Oriented Control is presented at the beginning. The chapter continues with the design of the speed and currents controllers. The controllers performances are tested and the results are shown. Next, the FOC using the measured position and speed rotor, is simulated and the results are presented and discussed.

In the forth chapter the sensorless control is introduced. Methods for rotor position and speed estimations are investigated. A method is chosen and the algorithm is presented. The method is simulated and tested at different conditions. The results are presented and discussed.

The fifth chapter presents the laboratory work. The setup is described along with the real time interface to dSpace. The experiments made are presented and discoussed.

The sixth chapter is the conclusions chapter. The whole work made in this project is concluded in the final chapter.

At the end of the report, the bibliography is presented and 3 Appendixes are attached.

A

Moment of inertia measurements

In order to design a proper control, some of the machine parameters have to be known accurately. The electrical parameters of the 2.2KW machine were read from the machine plate. Because the mechanical parameters were unknown, measurements were taken. The mechanical parameters, J,B and Td are presented in the mechanical equation, Eq.A.1

$$T_e = T_L + T_d + B\omega_m + J\frac{d}{dt}\omega_m \tag{A.1}$$

The moment of inertia J is an important parameter in the design of the speed controller, which makes the whole control of the machine to depend on it.

The setup for the mechanical parameters measurements is as shown in Fig.A.1.

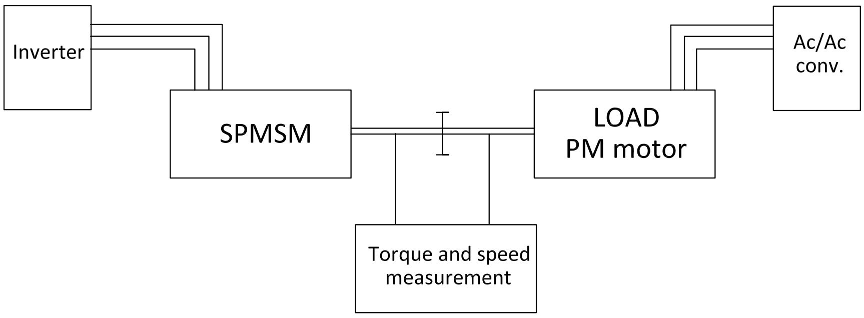

Figure A.1: *Setup for the measurements*

In order to determine the moment of inertia, the viscous friction B and the dry friction T_d have to be known. For calculating B and T_d, the torque is measured at two different speeds. The results are presented in TableA.1.

Speed	Torque
300 [rpm]	0.7 [Nm]
1500 [rpm]	1.05 [Nm]

Table A.1: *Measured speed and torque*

The viscous friction, B, is calculated using Eq.A.2.

$$B = \frac{T_{e1} - T_{e2}}{\omega_{m1} - \omega_{m2}} = 0.0028 \tag{A.2}$$

The dry friction, T_d is determined from the values from one level.

$$T_d = T_e - \omega_m B = 0.6102 \tag{A.3}$$

Next, a run out test is done in order to measure the moment of inertia, J. In Fig.A.2 the registered speed is presented.

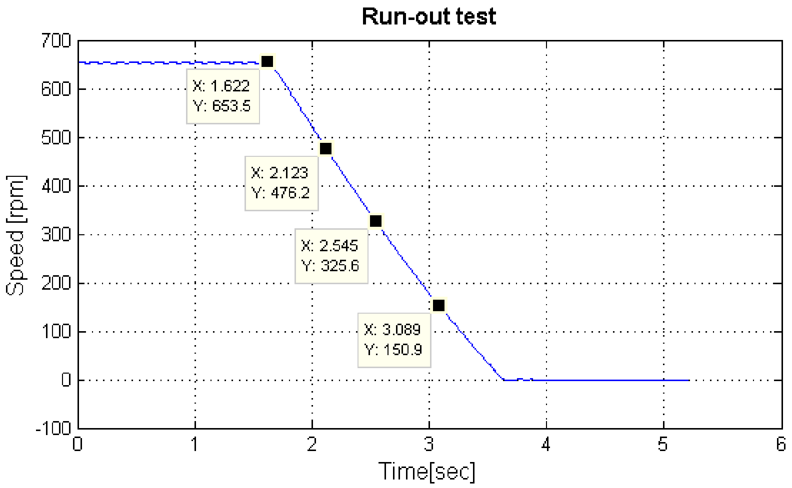

Figure A.2: *Setup for the measurements*

The machine was run at no load and the voltage was cut-off after approximately 1.6 sec. In order to determine the moment of inertia, four points are read from the speed curve such as the time interval between them is equal.

During the run-out test the produced (T_e) and the load torque (T_L) are zero. The moment of inertia is determined using Eq.A.4.

$$J = \frac{T_d + B\omega_m}{-\frac{d}{dt}\omega_m} \tag{A.4}$$

The moment of inertia is determined in three points and the mean value is taken. The data is presented in TableA.2.

The value of the moment of inertia is:

$$J = 0.019[kg \cdot m^2] \tag{A.5}$$

	Time [sec]	Speed [rpm]	Speed [rad/s]	Time difference [sec]	Speed difference [rad/s]	Moment of inertia [kg*m^2]	Moment of inertia mean value [kg*m^2]
Start point	1.622	653.5	68.43452				
Point 1	2.123	476.2	49.86766	0.501	-18.566856	0.020233073	0.019525314
Point 2	2.545	325.6	34.09683	0.422	-15.770832	0.018882531	
Point 3	3.089	150.9	15.80225	0.544	-18.294584	0.019460338	

Table A.2: *Data for J calculation*

B
System parameters

The main components of the Dspace system and their parameters:

- PM Synchronous Machine
  - rated power: 2.2[kW]
  - rated voltage: 285[V]
  - rated current: 6.1[A]
  - rated speed: 1750[rpm]
  - nominal frequency: 87.5[Hz]
- Danfoss VLT 5004 inverter
- Siemens SIMOVERT MC DC inverter type 6SE7022-6TC51-ZC23
  - rated voltage: input = 510 .. 650 V DC, output = [3 phase AC 0 .. 0.64] x input
  - rated output frequency = 0 .. 400 Hz
  - rated current: input = 30.4 A DC, ouput=25.5 A rms
  - rated power = 16.8 .. 20.3 kVA
  - switching frequency = 5 .. 10 kHz
- 2 LEM boxes.
- Siemens PMSM type ROTEC 1FT6084-8SH7:
  - rated power: 9.4 kW
  - rated torque = 20 Nm
  - rated current = 24.5 A
  - rated frequency = 300 Hz
  - rated speed = 4500 rpm.

C
Test journal

C.1 Motor operation at rated speed, rated torque

Purpose

To test the designed control - Field Oriented Control

Method

The machine was started with a step of $n = 1750[rpm]$. A step torque of 2[Nm] was applied at approximately 6[sec], and afterwards the torque was gradually increased to increased gradually to the rated torque $T_L = 12[Nm]$.

Results

The measured voltages and currents are represented in Fig.C.1 (a) respectively (b).

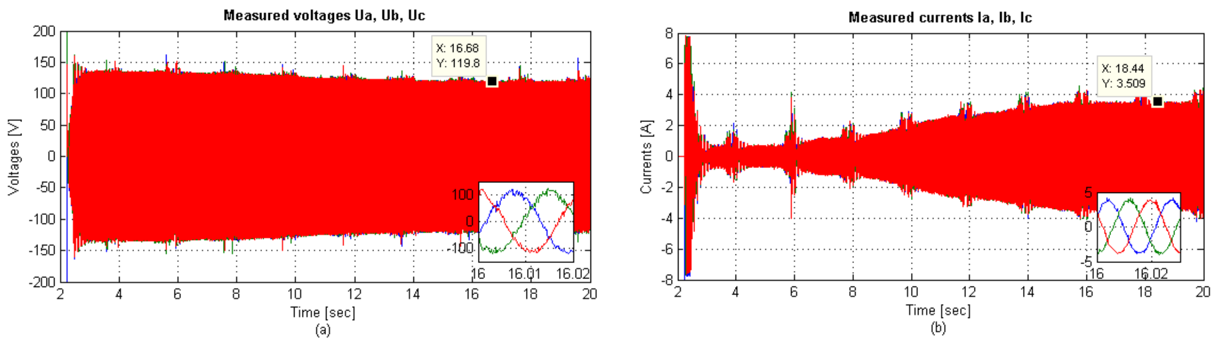

Figure C.1: *Measured values: (a) Voltages (b) Currents*

In Fig.C.2 the reference and the measured speed is presented.

Analysis of Results

The interest is in the measured currents Fig.C.1 (b). At 50% rated speed and nominal torque the amplitude of the currents is approximately 3.5[A].

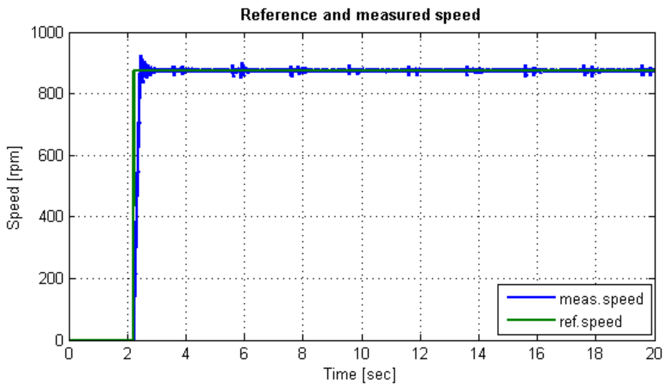

Figure C.2: *Reference and measured speed*

Errors

The value of the measured currents at rated torque is lower than the expected value 6[A].

Conclusions

A possible reason for the fact that there is a difference between the measured and the expected currents is that the load is not properly controlled and there is also a difference between the applied torque and the measured one.

D Simulation blocks

D.1 General presentation

The general presentation of the sensorless FOC and the PM synchronous machine is presented in Fig.D.1.

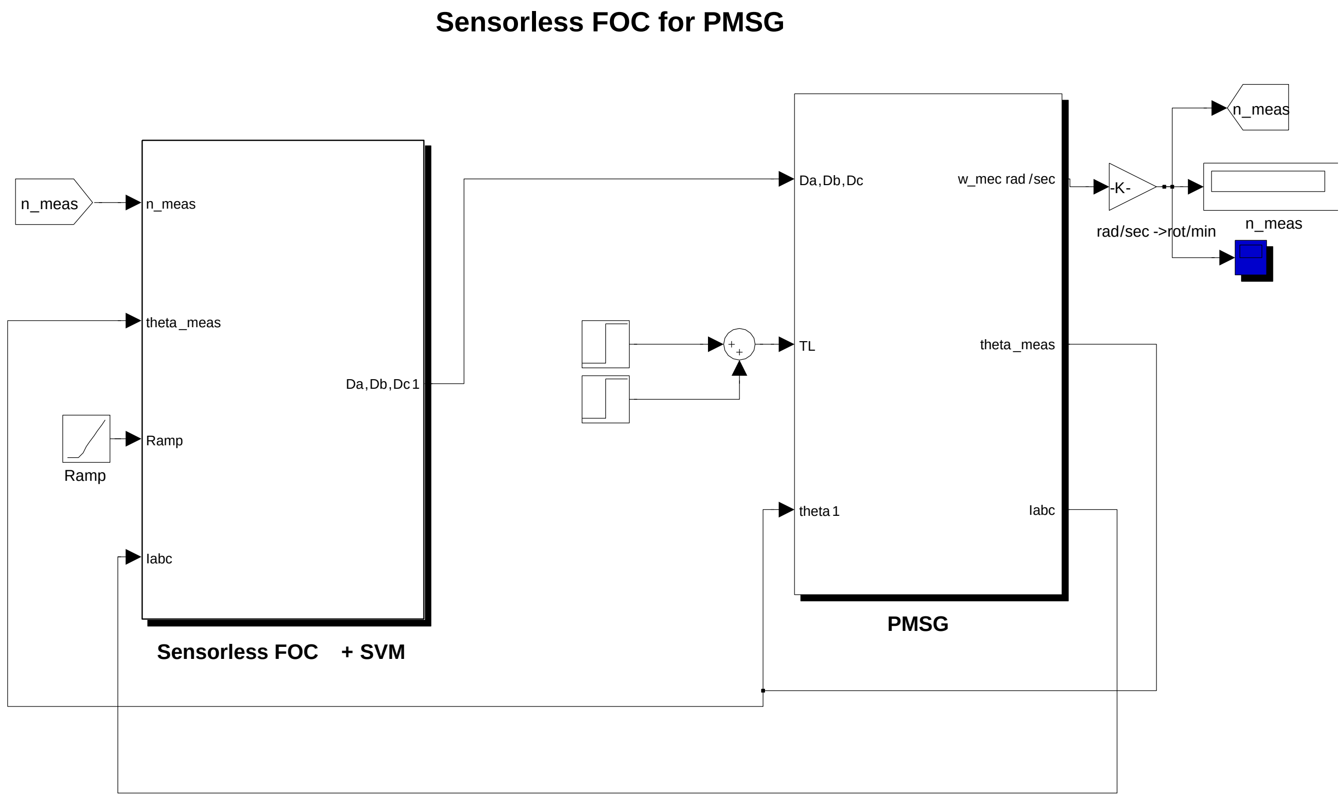

Figure D.1: *General structure of the simulation*

D.2 PMSM

The PM synchronous machine model from Simulink is presented in Fig.D.2.

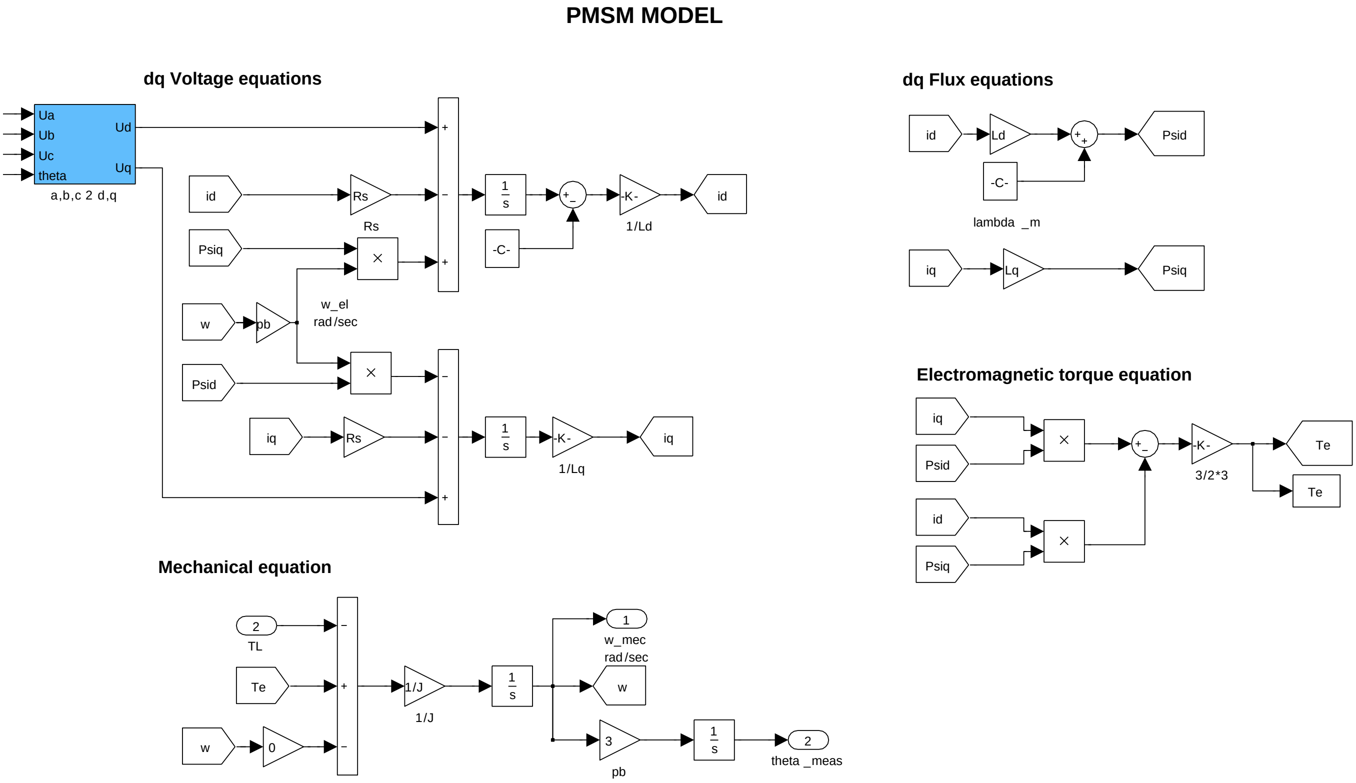

Figure D.2: *Simulink model of PM synchronous machine*

D.3 FOC

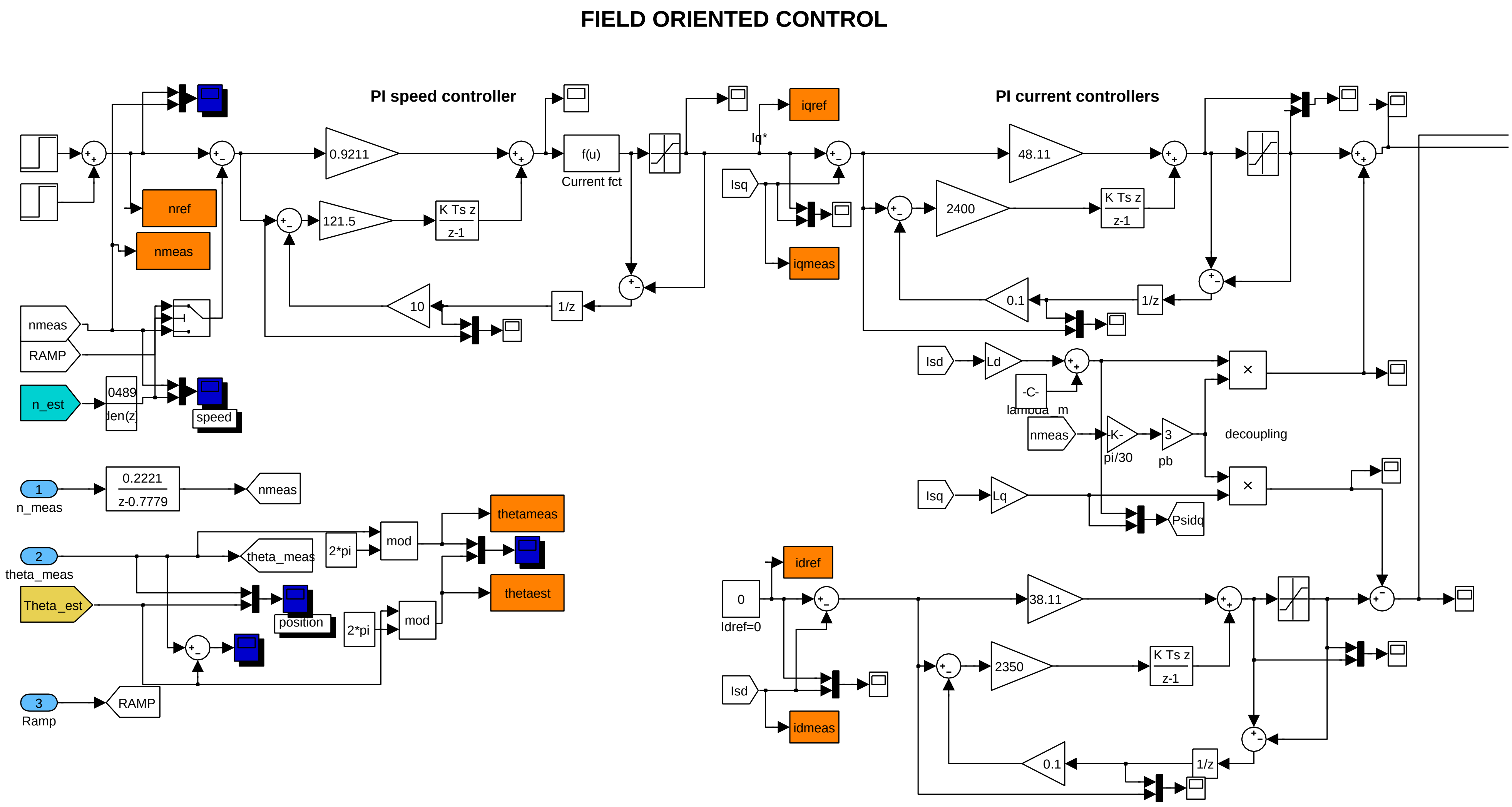

Figure D.3: *Simulink model of the FOC*